energies

MDPI

Article

Atomistic Investigations of Occupancy-Driven Structural Deformations in Binary H_2-THF Hydrates and Their Effect on Storage Capacity

Maryam W. Mohamed, Samuel Mathews, Alejandro D. Rey and Phillip Servio *

Department of Chemical Engineering, McGill University, Montreal, QC H3A 0C5, Canada; maryam.mohamed2@mail.mcgill.ca (M.W.M.); samuel.mathews@mail.mcgill.ca (S.M.); alejandro.rey@mcgill.ca (A.D.R.)

* Correspondence: phillip.servio@mcgill.ca; Tel.: +1-(514)-398-4400 (ext. 1026)

Abstract

Hydrogen is a clean fuel with the highest specific energy density and is central to net-zero goals, but its low volumetric energy density creates storage challenges that limit capacity and complicate deployment. Gas hydrates are hydrogen-bonded crystalline solids composed of water molecules forming polyhedral cages that trap gas molecules (guests). Pure hydrogen hydrates can achieve storage capacities comparable to or exceeding conventional systems and U.S. Department of Energy (DOE) targets, but their requirement for extreme pressures and low temperatures limits practical use. Thermodynamic promoters such as tetrahydrofuran (THF) substantially reduce formation pressures but displace hydrogen, therefore reducing capacity. We employ density functional theory (DFT) to examine how guest occupancy affects storage capacity in H_2-THF binary hydrates, leveraging atomic-level control not accessible experimentally. We identify a two-step structural response to increasing H_2 loading: an initial uniform lattice expansion that accommodates additional guests, followed by heterogeneous deformation that defines the upper occupancy limits. Using these occupancy ceilings, we find that binary hydrates can exceed DOE targets when THF loading is sufficiently low. These atomistic insights clarify the mechanisms underlying occupancy-driven structural behaviour and establish theoretical limits that can guide the design and optimization of hydrate-based hydrogen storage materials.

Keywords: hydrogen; gas storage; gas hydrates; thermodynamic promoters; tetrahydrofuran; density functional theory

Check for updates

Academic Editor: Chilou Zhou

Received: 2 May 2026
Revised: 23 June 2026
Accepted: 23 June 2026
Published: 26 June 2026

Copyright: © 2026 by the authors. Licensee MDPI, Basel, Switzerland. This article is an open access article distributed under the terms and conditions of the Creative Commons Attribution (CC BY) license.

1. Introduction

Gas hydrates are crystalline solids whose host framework consists of hydrogen-bonded water molecules forming polyhedral cages that trap guest gas molecules [1–4]. The van der Waals (vdW) interactions between the guest gas molecules and the water lattice contribute to the overall stability of the structure. The formation of these hydrates requires extreme conditions of high pressure and/or low temperature. The most common gas hydrate structures are structure I (sI), structure II (sII), and structure H (sH), each distinguished by the size and shape of water cages they are composed of [1]. The type of hydrate that forms is determined primarily by the nature of the gas molecules present in the system as well as the formation conditions [5]. Hydrogen (H_2) hydrates assume the sII structure, as first determined by Mao et al., which consists of small dodecahedral cages composed

of twelve pentagonal faces (denoted 5^{12}) and large hexakaidecahedral cages made up of twelve pentagonal and four hexagonal faces (denoted $5^{12}6^4$) [6].

Gas hydrates have high applicability to engineering solutions aimed at steering away from the use of fossil fuels. Most prominently, hydrates play an important role in hydrogen storage, which has been an obstacle to the widespread adoption of hydrogen as a clean fuel. While hydrogen has low volumetric energy density, it has the highest energy per unit mass of any fuel. Therefore, to make hydrogen practical for use, it must be stored in manageable form, which can be achieved by means of compression, liquefaction, or by trapping within other materials through forming chemical or physical bonds [7]. The efficiency of a hydrogen storage system depends not only on its storage capacity but also on its energy efficiency, i.e., the net usable energy remaining after both loading and unloading of hydrogen from the storage medium. Technologies such as compression, liquefaction, carbon nanotubes, metal hydrides, and ammonia face challenges due to limited storage capacity or poor energy efficiency [7].

Hydrates, on the other hand, have shown promising potential when it comes to hydrogen storage due to their safety, cost-effectiveness, efficiency, and low carbon footprint [7]. In fact, it has recently been shown that pure hydrogen hydrates can support volumetric capacities up to 0.075 kg H_2/L_{system} (9.5 wt%), surpassing the U.S. Department of Energy's (DOE) ultimate hydrogen storage target for onboard hydrogen storage systems for light-duty vehicles, which is set at 0.050 kg H_2/L_{system} (6.5 wt%) [8,9]. For pure hydrogen hydrates to be stable, they must form at extremely high pressures ranging from 180 to 600 MPa. To put it into perspective, at atmospheric pressure (0.1 MPa), stability would only be possible at temperatures below 140 K [10]. Such high pressures and/or low temperatures are necessary because hydrogen molecules are very small, and hydrate stability is strongly influenced by the size and shape of the guest molecule [11]. For hydrogen hydrates to be viable in practical applications such as automotive fuel storage, they must not only meet certain storage capacity targets but also be stable under moderate and safe conditions [12].

One strategy to address this challenge involves introducing thermodynamic promoters to hydrate systems [13]. One such promoter is tetrahydrofuran (THF), which has been demonstrated to reduce the formation pressure of hydrogen hydrates by nearly two orders of magnitude from 300 MPa to 7 MPa at 280 K [14]. The mechanism by which THF promotes the system is by acting as a guest itself and forming strong physical interactions in the form of hydrogen bonds with the host structure which stabilizes it [15]. Hydrogen can then diffuse into the stabilized structure, leading to the formation of binary H_2-THF hydrates [12]. This stabilizing effect of THF is so prominent that THF can form a stable sII hydrate at ambient pressure and around 278 K as the sole guest type even though THF molecules only occupy large cages due to their large size [14–16]. Therefore, THF serves a dual role: not only does it facilitate hydrate formation under milder pressures by acting as a secondary guest molecule, but its pure hydrate also functions as a valuable proxy for investigating gas hydrate behaviour under more practical conditions [17]. This, combined with the fact that THF exhibits the most pronounced promoting effect among other tested additives, warrants research attention on THF-promoted hydrate systems [18–20]. Nevertheless, the advantages of using THF as a thermodynamic promoter for hydrogen hydrate systems come with a trade-off: the presence of THF as a secondary guest reduces the overall hydrogen storage capacity of the system given that the THF molecules themselves occupy appreciable space in the hydrate [21]. This raises key questions regarding how the hydrate's storage capacity and properties are affected by the introduction of promoters, and whether the binary hydrate is a viable contender for hydrogen storage.

Stoichiometric binary H_2-THF hydrate refers to those compositions in which there is one THF molecule in each large cage in the structure. Experimental studies involving

gas release measurements, nuclear magnetic resonance (NMR), and neutron diffraction have differing conclusions on what the maximum H_2 occupancy in the small cages of these stoichiometric binary hydrates is, with some claiming single occupancy while others found evidence of multiple H_2 occupancy in small cages [11,14,21,22]. These discrepancies among experimental findings may arise from variations in quantification methods. For example, NMR data could be impacted by partial gas release during measurements, while direct measurements of hydrogen uptake and release are complicated by the relatively rapid evaporation of water and THF under the experimental conditions [21,23]. This highlights some of the difficulties faced during experimentation with hydrates.

Computational research has also played an important role in contributing to this debate. Alavi et al. employed molecular dynamics (MD) simulations to examine hydrogen occupancy in the small cavities, finding that hydrates containing either one or two hydrogen molecules per small cage possess similar configurational energies, though the single-occupancy structure consistently exhibits the lowest energy in all tested cases [10]. Grand Canonical Monte Carlo (GCMC) simulations provided additional insights into occupancy limits. These studies found that the most stable configuration corresponds to one THF molecule in each large cage and one hydrogen molecule in each small cage, leading to a total hydrogen content below 1.1 wt% within a temperature range of 250–300 K and pressures up to 350 MPa [12,24].

In addition to investigating hydrogen occupancy in the small cages of stoichiometric binary hydrates, the potential for hydrogen to co-occupy large cages alongside THF was also examined. Kaur and Ramachandran used dispersion-corrected density functional theory (DFT) to investigate the co-occupancy of hydrogen and THF within the large cages of the sII hydrate [25]. Their analysis of interaction energies and free energies associated with guest encapsulation indicated that co-occupancy of hydrogen and THF is thermodynamically feasible [25]. Similarly, Liu et al. used ab initio calculations of cohesive energies to show that the large cages can favourably accommodate one hydrogen molecule and one THF molecule [26].

Moreover, Lee et al. and Kim et al. proposed that lowering the THF concentration in the formation solution below stoichiometric composition (5.56 mol%) enables control over the fraction of large cages occupied by THF in the formed hydrate, a phenomenon termed as the tuning effect [27,28]. These nonstoichiometric binary hydrates would contain THF-free large cages that are capable of hosting clusters of hydrogen molecules, in addition to the small cages, thereby increasing the overall storage capacity of the system. Lee et al. reported that some large cages could accommodate up to four hydrogen molecules, forming a nonstoichiometric hydrate with a hydrogen storage capacity slightly exceeding 4 wt% [27]. However, there has been much disagreement on the tuning effect introduced by Lee et al. and Kim et al.

Using gas release measurements, NMR, and Raman spectroscopy, some experimentalists have claimed that hydrogen occupancy is independent of THF concentration [21,29]. Concurrently, other experimentalists were able to demonstrate evidence of the tuning effect in action by means of Raman spectroscopy, X-ray diffraction, and volumetric analysis, showing that by carefully adjusting the THF concentration, the hydrogen storage capacity of the system can be increased to approximately 3.4 wt% [5]. A potential factor contributing to the successful observation of the tuning effect in some experimental studies but not others is the hydrate formation method used. When starting from powdered ice and solid THF, as opposed to aqueous THF solutions, under hydrogen-pressurized conditions, the hydrogen molecules are more likely to occupy both small and large cages [5,29,30]. Computational studies have provided additional evidence supporting the tuning effect proposed by Lee et al. and Kim et al.: Using MD simulations, Zheng et al. and Kanaujiya et al. showed that

the thermodynamic stability of hydrate cages improves when hydrogen molecules occupy the THF-free cavities, demonstrating that gas storage capacity can indeed be tuned through THF concentrations [31,32]. Similarly, a recent MD study by Zhang et al. highlighted how adjusting THF levels directly impacts hydrogen capacity and hydrate grown rates [33]. They found that keeping the promoter concentration below the stoichiometric level is ideal for optimizing hydrogen loading in sII cages, in direct support of the tuning effect.

In this work, we investigate the effect of H_2 and THF occupancy on the structure and, in turn, the theoretical achievable hydrogen storage capacity, using zero Kelvin ab initio Kohn-Sham DFT as implemented in the Vienna Ab Initio Simulation Package (VASP) [34–37]. We contribute to the ongoing discussions on the occupancy limits in small and large cages in both stoichiometric and nonstoichiometric compositions of the binary hydrate from a DFT lens. Furthermore, we extend the analysis to identifying the response mechanisms by which the binary hydrate structures accommodate increasing guest occupancy as well as the transition away from this mechanism which signifies the onset of occupancy-induced structural failure. With DFT, we have superior control over the systems investigated down to the atomic level, allowing us to control composition and cage occupancy and investigate structural properties at the atomistic scale, such as bond length and angles, which would not be feasible through experimentation. Additionally, the first-principle nature of DFT makes it more accurate than other theoretical approaches that rely on empirical models. Nevertheless, in practice, DFT calculations are not exact since the exchange-correlation energy functional is not known exactly and must be approximated [38].

This paper is organized as follows. Section 2 describes the DFT methodology and simulation parameters, clarifies the nomenclature used to refer to different binary hydrate compositions, and introduces the oxygen classification scheme used for describing structural properties. Section 3 presents the results: first, the cohesive and binding energies are analyzed to assess overall thermodynamic stability, then distributions of geometric properties, such as cage volumes, bond lengths/interatomic distances, and interatomic angles, are examined across compositions to reveal the response mechanisms as the structures approach their occupancy limits. Section 4 combines the obtained results to formulate a theory on the failure mechanisms at play and discusses storage capacity. Section 5 culminates the key findings from this study. Additional data are provided in the Supplementary Materials.

2. Materials and Methods

2.1. Computational Details

Kohn-Sham DFT calculations were carried out with VASP 5.4.4 software, which requires an input of the initial structure [34–37]. The backbone (empty) sII hydrate unit cell structure was obtained from the X-ray diffraction study by Takeuchi et al. which consists of 136 water molecules, eight large ($5^{12}6^4$) cages, and sixteen small (5^{12}) cages [39]. Within this host framework, the water hydrogen atoms are arranged according to the Bernal-Fowler ice rules in a manner that minimizes the net dipole moment. The small and large cages were populated with H_2 and THF guest molecules using the geometric packing tool Packmol to generate the starting configurations for each tested composition [40]. For nonstoichiometric compositions, the choice of which large cages were to be THF-occupied was performed at random since our testing showed that symmetrically inequivalent occupancy patterns relax to degenerate ground state structures, as shown in Table S4 of the Supplementary Materials.

Each prepared structure was relaxed to its ground state in VASP by allowing cell shape, volume, and atomic positions to vary until both energy and force tolerances were satisfied. Simulations used a $1 \times 1 \times 1$ cubic unit cell, which produced well-converged results. A $1 \times 1 \times 1$ Gamma-centered k-point mesh was sufficient to sample the reciprocal space given the large simulation cell size. Electronic minimization used a mixture of the

blocked-Davidson and RMM-DIIS algorithms with an energy tolerance of 1 μeV, while geometric relaxation employed the conjugate gradient algorithm (CGA) with a force tolerance of 5 meV/Å. These simulation parameters were selected based on the results of the convergence tests presented in Supplementary Materials (Sections S1 and S2). Furthermore, this setup aligns with prior DFT literature encompassing various hydrate structures (sI, sII, and sH) with guest molecules of different sizes and polarities, including hydrogen, THF, carbon dioxide, and hydrocarbons (methane, ethane, propane, and butane) [8,41–46]. The applicability of these parameters across a broad spectrum of gas hydrate systems highlights their reliability for the present investigation.

VASP uses a plane-wave basis set with projector-augmented-wave (PAW) potentials to perform DFT calculations [47]. An energy cutoff of 520 eV is used to truncate the basis set, which is 30% above the maximum PAW cutoff for the species in the system, as recommended in the VASP documentation [48]. The revised Perdew-Burke-Ernzerhof (revPBE) exchange-correlation (XC) functional was used with DFT-D2 dispersion correction to account for the long-range interactions in the structure [49,50]. This specific functional and dispersion-correction combination is selected based on benchmarking against the pure THF and pure H_2 hydrate systems [8,43]. Because the revPBE + DFT-D2 framework has been independently validated for both these endpoint systems, it represents an optimal and physically transferable model for the intermediate H_2-THF hydrate systems considered in this study. All simulations were run on the Fir and Rorqual supercomputing clusters supported by the Digital Research Alliance of Canada.

2.2. Nomenclature and Oxygen Classification System

2.2.1. Naming Conventions for Stoichiometric and Nonstoichiometric Compositions of the H_2-THF Hydrate

Because numerous stoichiometric and nonstoichiometric binary hydrate compositions are investigated, a systematic naming convention is adopted to distinguish between them. For nonstoichiometric structures that permit THF-free large cages, n_{THF} denotes how many of the eight large cages in the unit cell are singly occupied by THF and therefore equals the number of THF molecules per unit cell; thus, it ranges from 1 to 7 for nonstoichiometric compositions. This parameter is equivalently referred to throughout this work as the "THF loading". Two additional composition parameters, n_s and n_L, specify the number of H_2 molecules per small cage and per THF-free large cage in the unit cell, respectively, i.e., they are the small- and large-cage H_2 occupancies. The total number of H_2 guest molecules, $N_{H_2,nonstoich.}$, in a nonstoichiometric unit cell is calculated as follows:

$$N_{H_2,nonstoich.} = 16n_s + (8 - n_{THF}) \cdot n_L \quad (1)$$

For stoichiometric compositions, a similar naming convention is applied, where n_{THF} is always equal to 8 to indicate that each of the eight large cages in the unit cell contains one THF molecule. However, n_L^* for stoichiometric compositions denotes the number of H_2 molecules co-occupying each large cage alongside THF, rather than the number of H_2 molecules in THF-free large cages, as in the nonstoichiometric cases. The parameter n_s retains the same definition in both frameworks, representing the number of H_2 molecules per small cage in the simulation cell. Accordingly, the total number of H_2 molecules in a stoichiometric unit cell is given by Equation (2).

$$N_{H_2,stoich.} = 16n_s + 8n_L^* \quad (2)$$

The general nomenclature used to refer to a particular composition is $\{n_s\}H_2(S)$-$\{n_L$ or $n_L^*\}H_2(L)$-$\{n_{THF}\}$THF. For example, $4H_2(S)$-$2H_2(L)$-3THF is the nonstoichiometric unit

cell containing three THF-occupied large cages, four H_2 molecules per small cage, and two H_2 molecules in each of the five THF-free large cages. In contrast, $4H_2(S)$-$2H_2(L)$-8THF denotes a stoichiometric composition with four H_2 molecules per small cage and two H_2 molecules in each of the eight large cages co-occupied with THF.

The weight fraction of hydrogen, w_{H_2}, in a structure of a given composition is given by Equation (3), where N_{THF} and N_{H_2O} are the total number of THF and H_2O molecules per simulation cell, respectively, which correspond to n_{THF} and 136 throughout this study. N_{H_2} corresponds to the total number of H_2 molecules per unit cell, as given by Equations (1) and (2), depending on whether the given structure is of nonstoichiometric or stoichiometric composition, respectively. M_x is the molecular weight of species x.

$$w_{H_2} = \frac{N_{H_2} \times M_{H_2}}{(N_{H_2} \times M_{H_2}) + (N_{THF} \times M_{THF}) + (N_{H_2O} \times M_{H_2O})} \quad (3)$$

2.2.2. Classification of Oxygen Atoms Based on Their Structural Environment

When examining changes in structural properties such as bond lengths and angles, it is useful to analyze not only their bulk behaviour over the entire unit cell but also their behaviour within specific localized regions. This approach makes it possible to identify where particular structural responses originate, which in turn helps clarify the underlying failure mechanisms. To enable a systematic analysis of this kind, a classification scheme is used to group water's oxygen atoms in the sII hydrate lattice into two categories based on the similarity of their local environments, in a similar approach to that taken by Mathews et al. for sI hydrates [51].

Class A oxygen atoms are those that belong to pentagonal faces and whose neighbouring oxygen atoms also belong to pentagonal faces, as illustrated in Figure 1a. That is, of the six polygonal faces that simultaneously share this type of water oxygen center, all of them are pentagons. Class B oxygen atoms are those that participate in hexagonal faces and whose neighbours could be part of either pentagonal or hexagonal faces. This type of oxygen atom is found in the water molecules forming hexagonal faces shared between large cages (Figure 1c) or pentagonal faces shared between small and large cages (Figure 1b). Thus, type B oxygen atoms may also be part of pentagonal faces, similar to type A atoms. The difference is that type A oxygen atoms are found only in pentagonal faces, whereas type B atoms appear in both pentagonal and hexagonal faces.

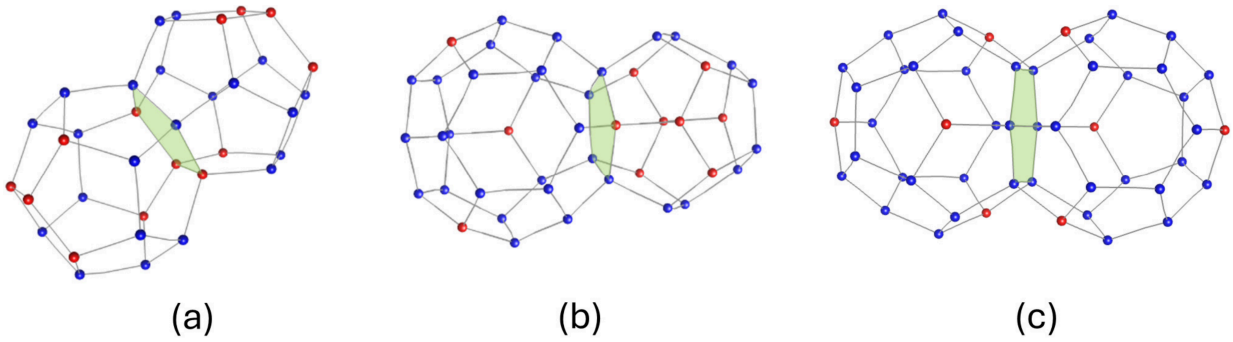


Figure 1. A visual representation of the two classes of oxygen atoms in the sII hydrate lattice and the different cage connections that exist. The red spheres represent class A oxygen atoms, and the blue spheres are class B. Water's hydrogen atoms are hidden for clarity. (**a**) Highlights the connection between two small cages through a pentagonal face; (**b**) highlights the connection between a small and a large cage through a pentagonal face; (**c**) highlights the connection between two large cages through a hexagonal face.

Of the 20 water molecules that compose a small cage, 12 of them contain B-type oxygen atoms and the remaining 8 are A-type. Thus, A-type and B-type oxygen vertices exist in a 2-to-3 ratio in small cages. On the other hand, 24 of the 28 water molecules making up large cages are those containing B-type oxygen atoms, leading to an A-to-B-type ratio of 1-to-6. Therefore, most of the A-type oxygen atoms are in the small cage environment, while the B-type oxygens are mostly representative of the large cage environment.

Based on this classification, structural parameters involving oxygen atoms, such as bond lengths and angles, can be further subdivided into distinct types according to the class of oxygen atoms involved. Each type corresponds to a specific local region within the hydrate lattice, allowing differences in their behaviour to reveal whether various parts of the structure respond differently to variations in composition. A summary of the structural properties that can be discretized in this manner is presented in Figure 2. It should be noted that the A-B-A permutation of the O-O-O angle does not occur in the sII hydrate lattice, which is why only five unique O-O-O angle types are shown.

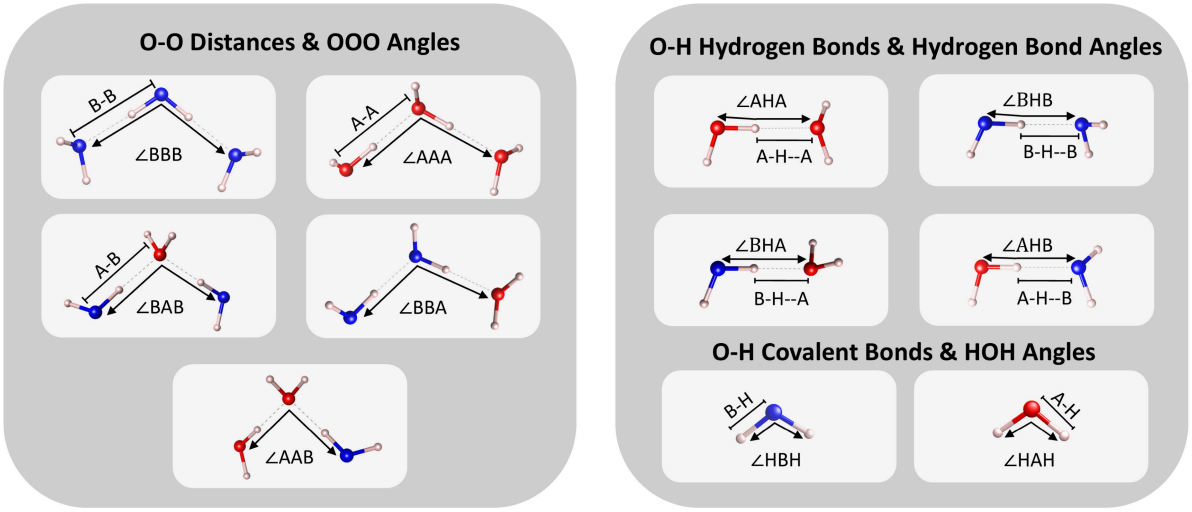


Figure 2. The different types of interatomic distances/angles and bond lengths/angles based on the classes of the oxygen atoms involved. The red spheres are class A oxygens, the blue spheres are class B oxygens, and the white spheres are hydrogen atoms.

2.3. Interatomic Distances and Angles

In the subsequent analysis of how cage occupancy and THF loading influence the binary hydrate structure, various interatomic distances, bond lengths, and interatomic and bond angles are examined through their mean distributions, standard deviations, and sensitivities to occupancy.

To calculate the bond length or interatomic distance between two atoms, X and Y, with Cartesian coordinates (x_1, y_1, z_1) and (x_2, y_2, z_2), respectively, the Euclidean distance formula is applied.

$$d = \sqrt{(x_2 - x_1)^2 + (y_2 - y_1)^2 + (z_2 - z_1)^2} \tag{4}$$

To determine the angle defined by three atoms, $X(x_1, y_1, z_1)$, $Y(x_2, y_2, z_2)$ and $Z(x_3, y_3, z_3)$, where Y is the central atom, the Euclidean distances between X and Y (d_1), and Z and Y (d_2) are first calculated using Equation (4). The included angle θ is then obtained according to the definition of the dot product between two vectors.

$$\theta = \cos^{-1}\left(\frac{\vec{YX} \cdot \vec{YZ}}{d_1 d_2}\right) \tag{5}$$

For this analysis, it is useful to establish reference values for comparison, which are based on the corresponding properties in the empty sII hydrate. Table S3 of the Supplementary Materials summarizes these reference values. Because trends across nonstoichiometric THF loadings are consistent, we only present the two limiting cases here, namely $n_{THF} = 1$ and $n_{THF} = 7$. The full dataset is provided in Section S5 of the Supplementary Materials.

3. Results

3.1. Energy Analysis

Because DFT simulations occur at 0 K, the thermal entropic contribution (TS) is zero, and the calculated total energies directly represent the static Gibbs free energy landscape of the systems considered. The cohesive energy is calculated from the ground state total energies of the enclathrated binary hydrate structures and its isolated constituents according to Equation (6). E_{H_2-THF} is the ground state energy of the binary sII hydrate of a given composition, while E_{H_2}, E_{H_2O}, E_{THF} are the ground state energies of isolated hydrogen, water, and THF molecules, respectively. N_{H_2}, N_{H_2O}, N_{THF} are the total numbers of hydrogen, water, and THF molecules per unit cell, respectively.

We analyze cohesive energy rather than absolute total energy because the latter is an extensive quantity that changes with system size as well as with thermodynamic stability. That means differences in total energy with composition cannot be unambiguously attributed to stability. On the other hand, cohesive energies are computed relative to a common baseline, i.e., the energies of the isolated constituents, which removes the extensive dependence on system size and isolates the chemically meaningful energy change associated with forming the structure.

$$E_{cohesive} = E_{H_2-THF} - \left[\left(N_{H_2} \cdot E_{H_2}\right) + \left(N_{H_2O} \cdot E_{H_2O}\right) + \left(N_{THF} \cdot E_{THF}\right)\right] \quad (6)$$

Based on this definition of cohesive energy, a negative value indicates a stable system that favourably forms from its constituents. The cohesive energies of compositions corresponding to different configurations of small- and large-cage occupancies are shown in Figure 3.

The cohesive energies of all computationally converged structures are negative, indicating thermodynamic stability and supporting the robustness of our simulation parameters resulting in the reliable identification of relatively stable structures.

Furthermore, for any THF loading, at a fixed large-cage H_2 occupancy, the cohesive energy decreases (becomes more negative) as the first H_2 molecule is added to the small cages, i.e., incrementing n_s from 0 to 1 for a given n_L or n_L^*, which indicates increased stability. Upon further increase in the small-cage occupancy, however, cohesive energies start to increase (become less negative), as a result of growing repulsive forces. This phenomenon was also observed through MD and DFT studies on H_2-THF hydrates, and on pure H_2 hydrate systems [8,10,25,31]. This becomes more evident upon inspecting the binding nature of the small-cage H_2 guests, which is reflected by the binding energy given by Equation (7). This binding energy is a measure of the added guest-guest and guest-host interactions that form upon incrementing the H_2 small-cage occupancy. $E_{H_2\ -\ THF}$ is the total energy of a given binary hydrate composition (stoichiometric or nonstoichiometric), and $E_{residue(SC)}$ is the total energy of the binary hydrate of the same large-cage occupancy and THF loading but with one less H_2 per small cage (n_s).

$$E_{binding,H_2(SC)} = E_{H_2-THF} - \left[E_{residue(SC)} + \left(16 \cdot E_{H_2}\right)\right] \quad (7)$$

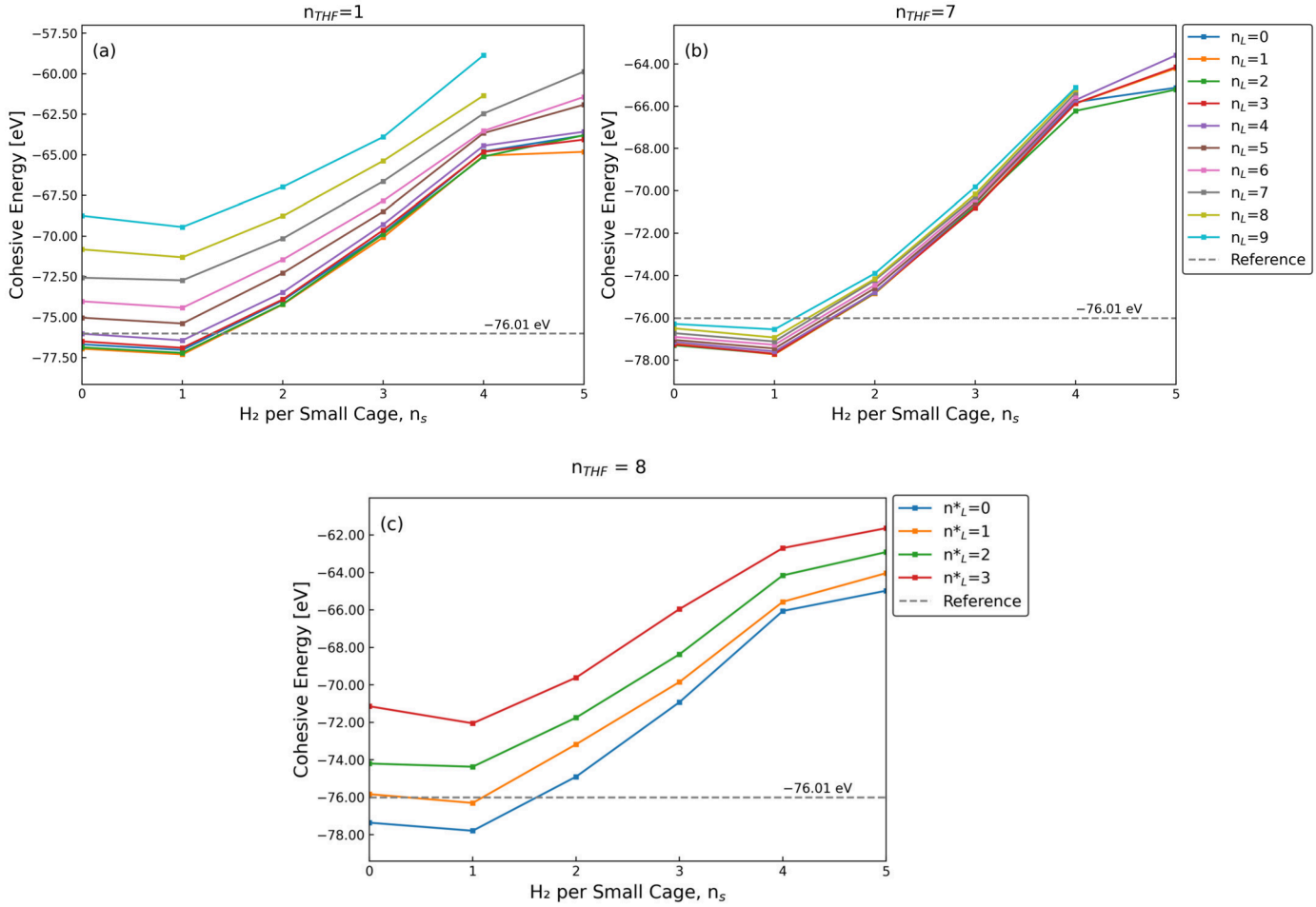


Figure 3. Cohesive energies of nonstoichiometric compositions under the THF loadings of (**a**) 1 and (**b**) 7, and (**c**) stoichiometric compositions as a function of small-cage occupancy. Each level curve presented corresponds to a given large-cage occupancy. The reference line indicates the cohesive energy for the empty sII hydrate.

Given this definition, a negative binding energy corresponds to net attractive forces brought about by the addition of a H_2 molecule to the small cages, whereas a positive binding energy implies overall repulsive forces. As presented in Figure 4, only configurations with $n_s = 1$ exhibit negative binding energies as per Equation (7). Parallel findings from classical MD simulations indicate that this phenomenon is also observed at non-zero temperatures [10]. The binding energies become positive and increase in magnitude up to $n_s = 4$ for both stoichiometric and nonstoichiometric compositions, after which they experience a sharp drop in magnitude. This corresponds to the regions in Figure 3 where the cohesive energy level curves become flatter, indicating a reduced sensitivity to small-cage H_2 occupancy.

The decrease in the magnitude of the binding energy going from $n_s = 4$ to 5 while still being positive indicates that the addition of the fifth H_2 molecule to the small cages continues to produce net repulsive forces, but not with as much strength as its predecessors. This signifies that the confined volume of the small cages is somehow disrupted, thus creating more free space for the H_2 molecules in small cages to exist and accordingly reducing repulsive interactions. The reduced sensitivity of cohesive energies over the same range of small-cage occupancies supports this conclusion. At this stage, we hypothesize that two different mechanisms are at play in response to increasing small-cage occupancy: one that accommodates the increasing repulsive interactions while maintaining overall structural integrity, which can no longer be sustained beyond $n_s = 4$, and another that

marks the onset of structural deformation at the small-cage level. This will become more apparent from the analysis of geometric parameters in the following sections.

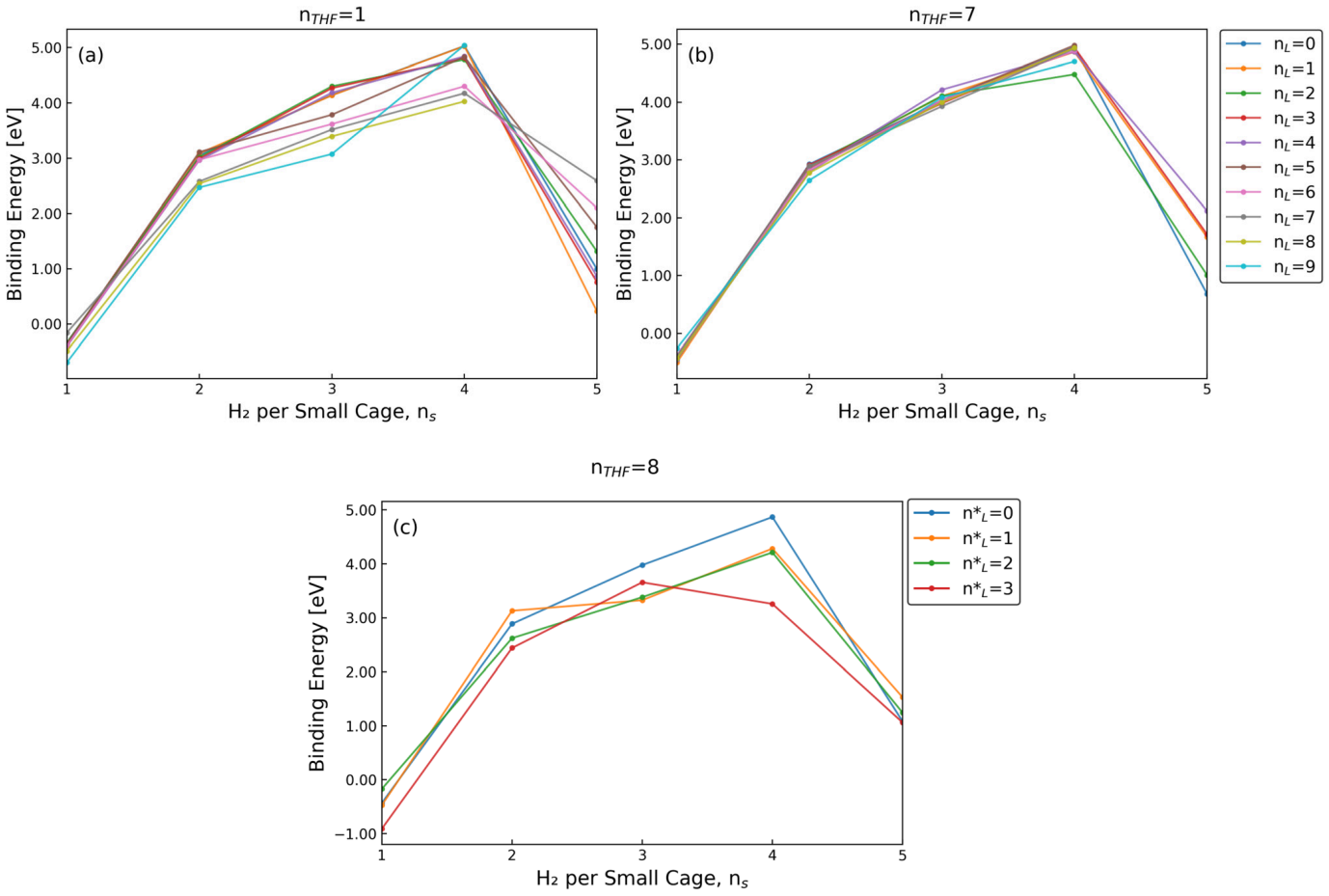


Figure 4. The binding energies corresponding to incrementing the small-cage H_2 occupancy for nonstoichiometric compositions under the THF loadings of (**a**) 1 and (**b**) 7, and for (**c**) stoichiometric compositions according to Equation (7).

Similarly, the binding energies associated with increasing the large-cage H_2 occupancy in stoichiometric (n_L^*) or nonstoichiometric (n_L) compositions can be determined. The results are plotted in the Supplementary Materials Figures S11 and S12. For nonstoichiometric compositions, there is no consistent pattern of how increasing H_2 occupancy in the THF-free large cages impacts the binding energy across different THF loadings and for different small-cage H_2 occupancies. This highlights the complex coupling between H_2 occupancy in THF-free large cages and both small-cage H_2 occupancy and THF loading. For stoichiometric compositions, increasing the number of H_2 molecules co-occupying large cages with THF consistently results in positive binding energies as shown in Figure S12 of the Supplementary Materials, highlighting that large cages occupied by THF are energetically favoured to remain free of H_2 rather than to be co-occupied. One thing to note as observed from Figure 3a,b is that the sensitivity to n_L, which is depicted by the vertical spacing between level curves, decreases as THF loading increases. This reduced sensitivity arises because at high THF loadings, the low fraction of hydrogen-occupied, THF-free large cages means that they are more dispersed in the bulk structure, and changes in their H_2 content have minimal effects beyond their local environment.

The impact of THF loading can be assessed using the binding energy calculated according to Equation (8), where $E_{THF,hydrate}$ is the total energy of a pure sII THF hydrate

(that is, not containing any H_2 guest molecules) at a given loading, and $E_{empty\ hydrate}$ is the total energy of the empty sII hydrate, in which there are no guest species of any type.

$$E_{binding,THF} = E_{THF\ hydrate} - \left[E_{empty\ hydrate} + (N_{THF} \cdot E_{THF})\right] \quad (8)$$

Figure 5 illustrates how this binding energy follows a decreasing trend as the THF loading per unit cell is increased. This binding nature of THF is characteristic of it being a thermodynamic promoter and contributes to the overall stability of the structure even as the repulsive forces grow with increasing hydrogen occupancy. Therefore, it is the combined effect of H_2 in small cages, H_2 in large cages, and THF that determines whether a structure of given composition is overall stable or not relative to its constituents, as given by the cohesive energies. These results are in agreement with the MD studies performed by Liu et al. and Alavi et al. in which they also observed the stabilizing effect of THF on the structure based on cohesive energy trends [10,26].

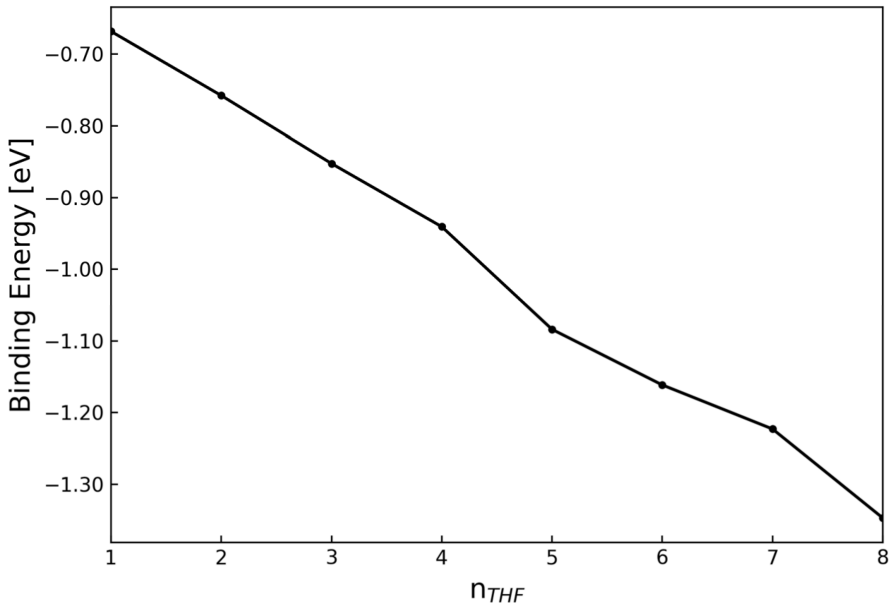


Figure 5. Binding energies of pure sII THF hydrates at different THF loadings according to Equation (8).

3.2. Geometric Analysis

3.2.1. Cage Volumes

The average small- and large-cage volumes in the unit cells of stoichiometric and nonstoichiometric compositions are presented in Figures 6 and 7. These cage volumes were determined using the standard convex hull method. The overall trend observed is that of an expansion of the small and large cages as both small- and large-cage occupancies increase, as highlighted by the positive slopes of the level curves and their upward shift from one large-cage occupancy to a higher. The connectivity between the small and large cages in the structure, as depicted in Figure 1, means that the expansion in one cage type induces an expansion in the other due to shared faces. This is in line with what was observed for pure H_2 hydrates with increasing occupancies [8]. The expansion trend aligns with finite-temperature MD studies of H_2-THF hydrates, which show that single H_2 occupancy in small cages causes negligible volume change [10]. This is reflected in Figures 6 and 7, where the level curves exhibit near-zero slopes between $n_s = 0$ and $n_s = 1$.

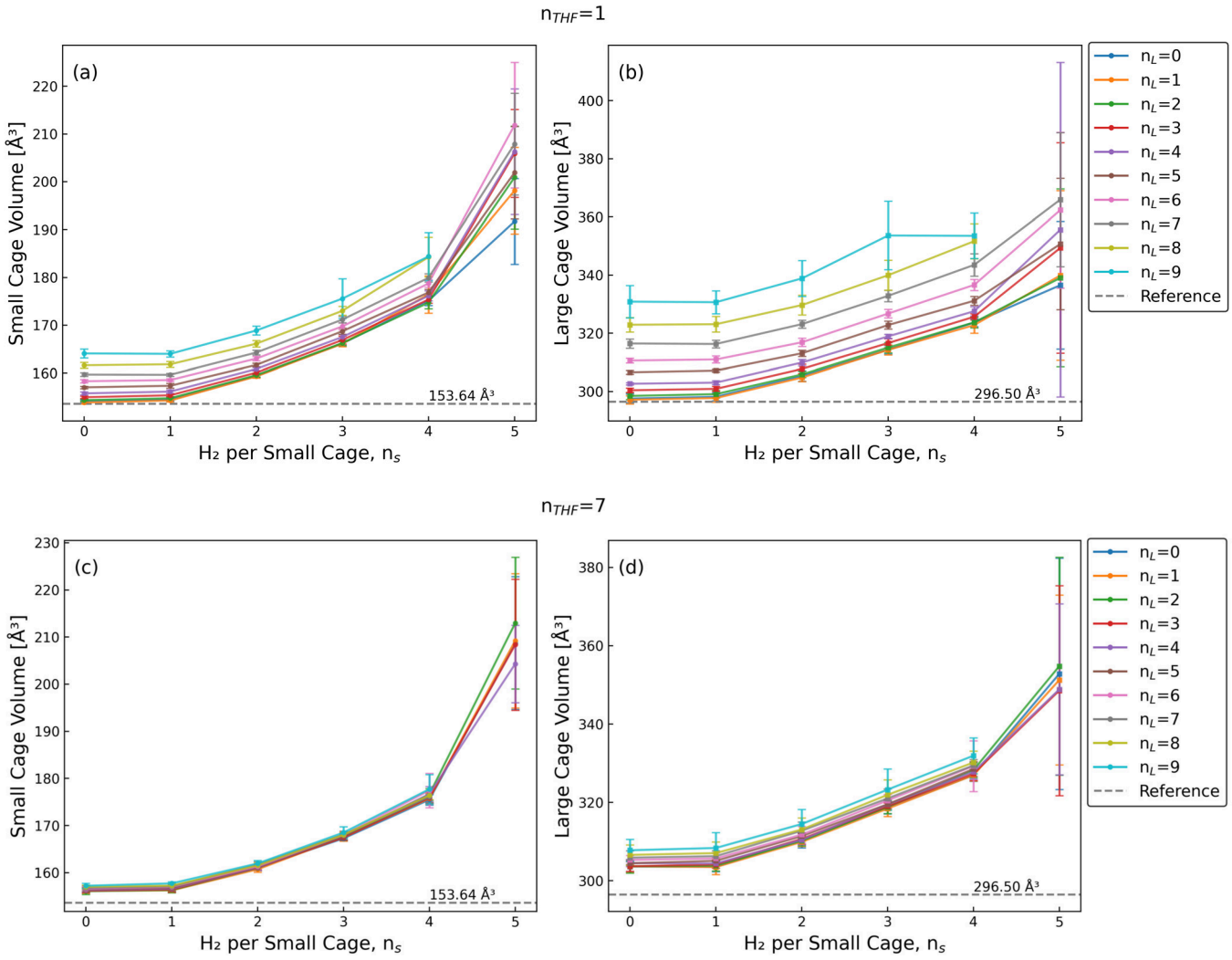


Figure 6. Average small- and large-cage volumes for nonstoichiometric compositions under the THF loading schemes of 1 (**a**,**b**) and 7 (**c**,**d**). The vertical bars represent the spread of the distributions around their average. The reference lines indicate the average small- and large-cage volumes for the empty sII hydrate.

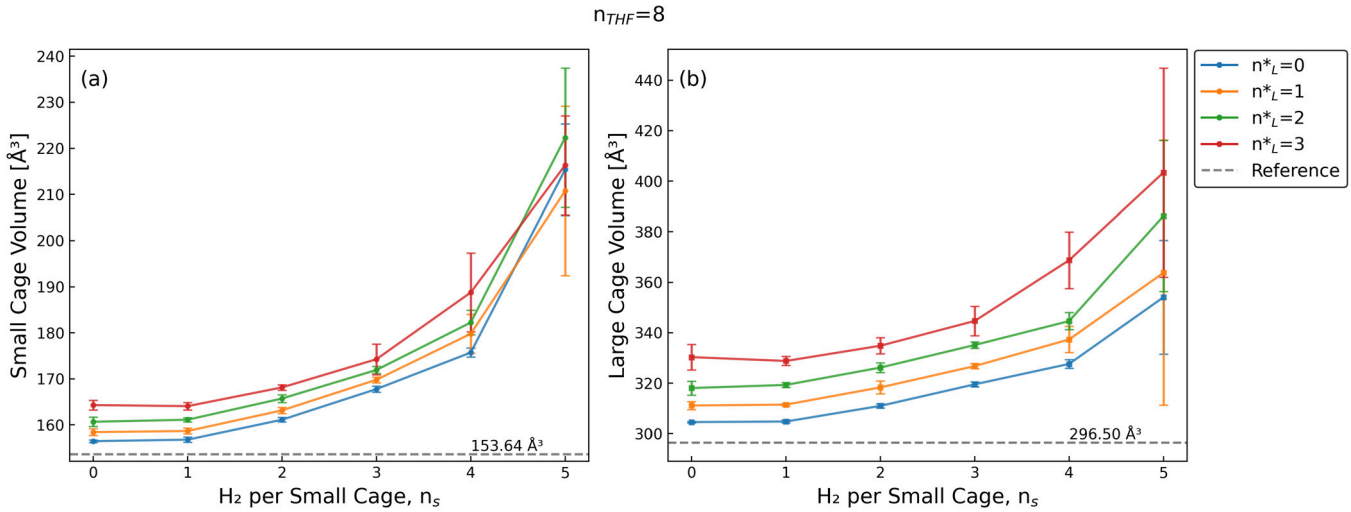


Figure 7. Average small (**a**)- and large (**b**)-cage volumes for stoichiometric compositions. The vertical bars represent the spread of the distribution around the average. The reference lines indicate the average small- and large-cage volumes for the empty sII hydrate.

The small-cage volumes are less sensitive to the large-cage occupancy than the large-cage volumes are (compare the vertical spacing between the level curves of Figure 6a,b and similarly compare Figure 6c,d). This is because large cages have more free space available to accommodate H_2 molecules and can reach higher occupancies before their volume expansion is appreciable to start influencing the small-cage volumes.

Additionally, as observed with the cohesive energy trends, the sensitivities of the small- and large-cage volumes with respect to the large-cage occupancy decrease with increasing THF loading as can be seen by comparing the vertical spacing between level curves in Figure 6a,c as well as in Figure 6b,d. The level curves being nearly parallel in Figure 6, as well as in Figure 7, indicates a similarity in the cage expansion mechanism across different THF loadings (n_{THF}) and for different large-cage occupancies (n_L *or* n_L^*) up until the small-cage occupancy associated with widened distributions. In fact, this near-independence of property sensitivity to small-cage H_2 occupancy from large-cage H_2 occupancy and THF loading recurs across the properties examined in this study and has also been noted by Zheng et al. and Liu et al. in their MD studies of similar systems [26,31].

Evidently, the primary structural response to increasing H_2 occupancy is uniform expansion of the cages to create more free space for their accommodation. However, this mechanism reaches its threshold at high small-cage occupancies that are characterized by wide distributions represented by the vertical bars. The widening of these distributions around the means indicates the destabilization of the structures as they approach their occupancy limits. It becomes more apparent how this structural degradation takes place upon investigating bond lengths and angles across the unit cell.

The cage volume trends observed for the stoichiometric compositions with increasing small-cage occupancy are similar to those for nonstoichiometric compositions. In addition, we notice wide distributions when $n_L^* = 3$, even at lower small-cage occupancies, hinting that at high co-occupancy levels, the deformations are instigated at large cages rather than small cages.

3.2.2. O-O Distances

The O-O distance is the separation between oxygen atoms belonging to adjacent water molecules in the hydrate lattice. Hence, it is a measure of how distant the water molecules are from each other. By examining the variation in these distances, specifically those categorized based on the types of oxygen atoms involved, we can get a more refined understanding of the occupancy-driven effects on the structure. The general trend observed across all types of O-O distances within nonstoichiometric and stoichiometric structures is one of monotonic increase with both small- and large-cage occupancy as presented in Figure 8. This is reasonable based on the cage volume trends from which it was concluded that an increase in occupancy causes an expansion of both small and large cages, driving the water molecules apart, and elongating the O-O distances.

Each O-O distance type has its own baseline (taken as the average value in the empty sII hydrate) because regions of the sII lattice are subject to different geometric constraints that affect local packing arrangements of the water molecules. A-A distances are unique to the pentagonal faces shared exclusively between two small cages; A-B distances are found in the pentagonal faces shared between small cages as well as between small and large cages; B-B distances are mostly concentrated in pentagonal faces joining small and large cages as well as in hexagonal faces joining large cages. The baseline A-A, A-B, and B-B distances are 2.693 Å, 2.715 Å, and 2.723 Å, respectively. Thus, the B-B distances are longer than the A-B distances, which in turn are longer than the A-A distances.

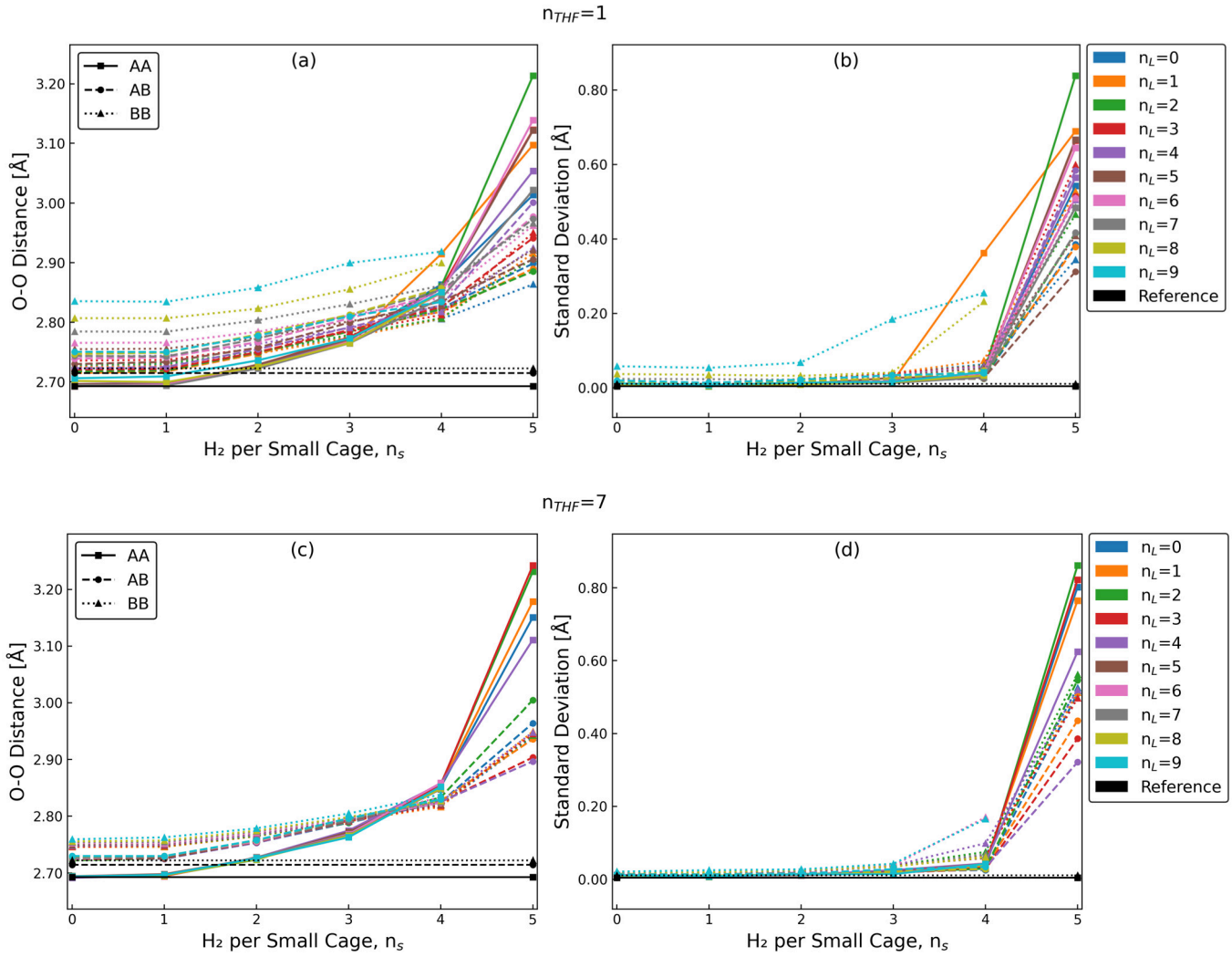


Figure 8. Average O-O distances classified by the different types of oxygen atoms for nonstoichiometric compositions corresponding to a THF loading of (**a**) 1 and (**c**) 7 and their standard deviations (**b**,**d**). The reference lines indicate the average values of the different O-O distances and their corresponding standard deviations based on the empty sII hydrate structure, as tabulated in Table S3 of the Supplementary Materials.

Once guest molecules are introduced to the system, new types of interactions form, namely guest-guest and guest-host interactions, but even the pre-existing host-host interactions get impacted by the presence of guest molecules. Thus, it is expected that the water lattice will experience changes from these baseline values as more guest molecules are incorporated. This effect is evident from shifts in the O-O distances relative to their baselines even in pure THF hydrates (i.e., when no H_2 guests are present, corresponding to $n_s = 0$ and $n_L = 0$ or $n_L^* = 0$). The deviation between each O-O distance in these pure THF hydrate structures and its corresponding baseline represents the minimum offset attributable solely to THF as a guest molecule and thus isolates the promoter's influence on the hydrate lattice.

As depicted in Figure 9, the B-B distances show the largest offset from their baseline, followed by the A-B and then A-A distances. This is a result of the THF molecules existing in the large cages only, thus the large cages expand the most under direct impact, followed by the indirect small-cage expansion, which explains the orders of magnitude of the relative O-O distances given that the large-cage faces are predominantly characterized by B-B and A-B distances rather than A-A distances. This is also in accordance with the cage volume

sensitivity trends which revealed that small-cage volumes are less sensitive to large-cage occupancy than large-cage volumes.

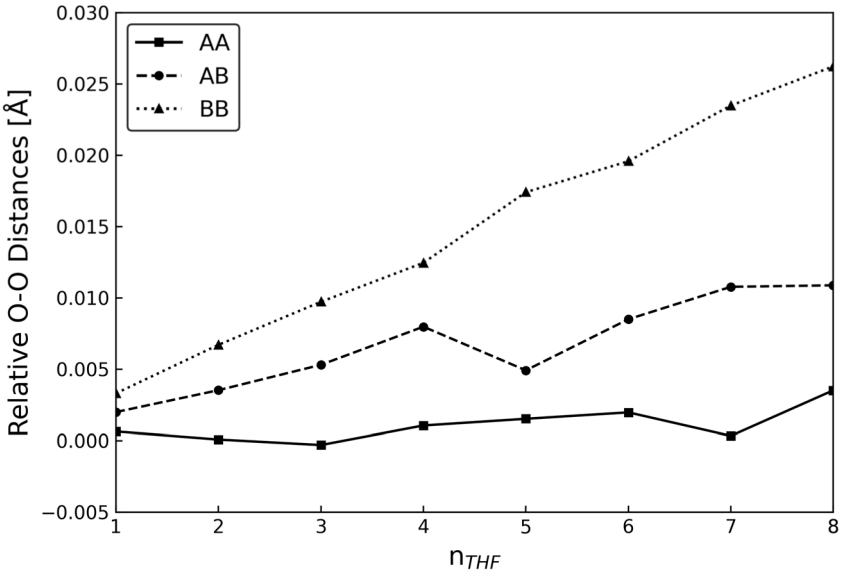


Figure 9. The difference between the O-O distances of pure THF hydrates ($n_s = 0, n_L, n_L^* = 0$) at different loadings and the corresponding reference distance based on the empty sII hydrate structure.

The A-B and B-B offsets also increase with increasing THF loading, while the A-A offset fluctuates around zero. Moreover, at a given THF loading, the A-B and B-B distances are more sensitive to the H_2 large-cage occupancy, as given by the wider vertical spacing between their level curves in Figure 8a,c, whereas the A-A distances are the least sensitive. This corroborates the claim that A-A distances are more influenced by changes local to the small cages, while A-B and B-B distances capture changes to the large cage geometries as well as interactions between small and large cages. Nevertheless, as with the energies and cage volumes, the effect of large-cage H_2 occupancy on the A-B and B-B distances diminishes as THF loading increases due to the reduced fraction of hydrogen-occupied large cages, which explains why the level curves collapse toward each other when comparing Figure 8a,c. Thus, at higher THF loadings, the structural properties are mostly impacted by the small-cage H_2 occupancy and the THF loading itself.

The previously outlined trends are consistent while the standard deviations are small. However, this behaviour becomes inconsistent once the distributions widen significantly, as given by increased standard deviations shown in Figure 8b,d. The standard deviation reveals how uniform a property is across the structure: a narrow distribution indicates a uniform, ordered structure, while a wide distribution is a sign of heterogeneity and local distortions. This is what is seen to occur beyond a small-cage occupancy of 4, or even earlier in some cases, at lower THF loadings. The structure is able to uniformly accommodate the increase in H_2 occupancy by expansion up until the point of significant widening in the distributions. At the threshold, water molecules are forced sufficiently apart that cages begin to deform: polygonal faces lose their defining geometry as water molecules become less tightly bound and undergo angular reorientation and positional displacement during relaxation. Further evidence for this mechanism appears in the O-H covalent and hydrogen bond length changes and in the O-O-O angle distributions presented in forthcoming sections.

Where the distributions start to widen significantly, we notice that the A-A distances experience the widest spread, signifying that the small cages are the first to undergo significant deformation. This indicates that occupancy-driven deformation initiates in the

small cages, which sets off a cascade: distortions begin in the small cages, which then perturb the shared faces and propagate deformation into neighbouring large cages. Because n_L can rise to 8 or 9 before distributions widen appreciably when small cages contain fewer than 4 H_2 molecules, the small-cage occupancy primarily governs structural stability for nonstoichiometric compositions.

The occupancy-driven onset of structural failure creates openings in the cage faces that permit inter-cage relocation, allowing H_2 to shift from strained small cages into adjacent large cages. As shown in Figure 10, pentagonal faces connecting small and large cages experience geometric breakdown when n_s reaches 5, enabling H_2 transfer to larger cavities and reducing the occupancy in some small cages back to 4.

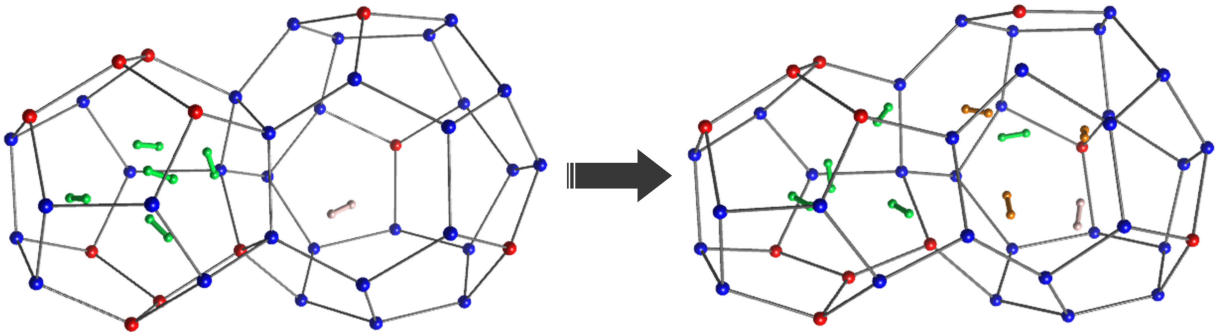


Figure 10. An instance of H_2 relocation from small cages to a large cage in a structure of nonstoichiometric composition corresponding to $n_s = 5$, $n_L = 1$, and $n_{THF} = 1$. The cage pair prior to relaxation is shown to the left of the arrow, and the converged structure appears on the right. The green H_2 molecules are those initially belonging to the small cage depicted here. The orange H_2 molecules originated from other neighbouring small cages not pictured. The white H_2 molecule is the one originally belonging to the large-cage visible here. The red and blue spheres represent class A and class B oxygen atoms, respectively. Water's hydrogen atoms are hidden for clarity.

Zheng et al., using MD simulations at 12 MPa and 270 K, reported the onset of inter-cage hydrogen migration at a small-cage occupancy of 2 H_2 molecules [31]. To provide deeper mechanistic insight into this behaviour, Gorman et al. also investigated H_2-THF hydrates at 5 MPa and temperatures up to 250 K [52]. They observed that at lower temperatures, guest molecules undergo intra-cage displacement, in which they remain within the same cavity they started in and just move closer to the cage faces, causing their geometric distortion. Inter-cage migration was found to occur at higher temperatures (250 K) for the structures with doubly occupied small cages.

In contrast, 0 K DFT calculations are inherently static due to the absence of thermal effects, and so they do not capture the dynamic inter/intra-cage migration phenomena modeled in MD simulations. However, DFT calculations can capture the thermodynamic endpoints. Thus, the occupancy limits identified in this study are inherently higher and represent theoretical upper bounds. Nevertheless, extreme loadings result in mechanical strain and repulsions between guests that mimic the thermal destabilization observed in finite-temperature MD studies. When these initial configurations with crowded cages undergo geometric optimization, the system minimizes its energy by relaxing into a final state where some hydrogens have undergone a coordinate shift to adjacent, less-strained cavities. These final relaxed structures produced via DFT are conceptually equivalent to the stable configurations resulting from MD simulations, confirming that these configurations are energetically favoured states. Additionally, classical MD relies on empirical modeling of atomic interactions impacted by the accuracy of the force fields used, unlike first-principle DFT calculations. This introduces an inherent difference in methodologies that could be another source of the discrepancy between results.

Similar trends with respect to the small-cage occupancy are observed for stoichiometric compositions as shown in Figures 11 and 12.

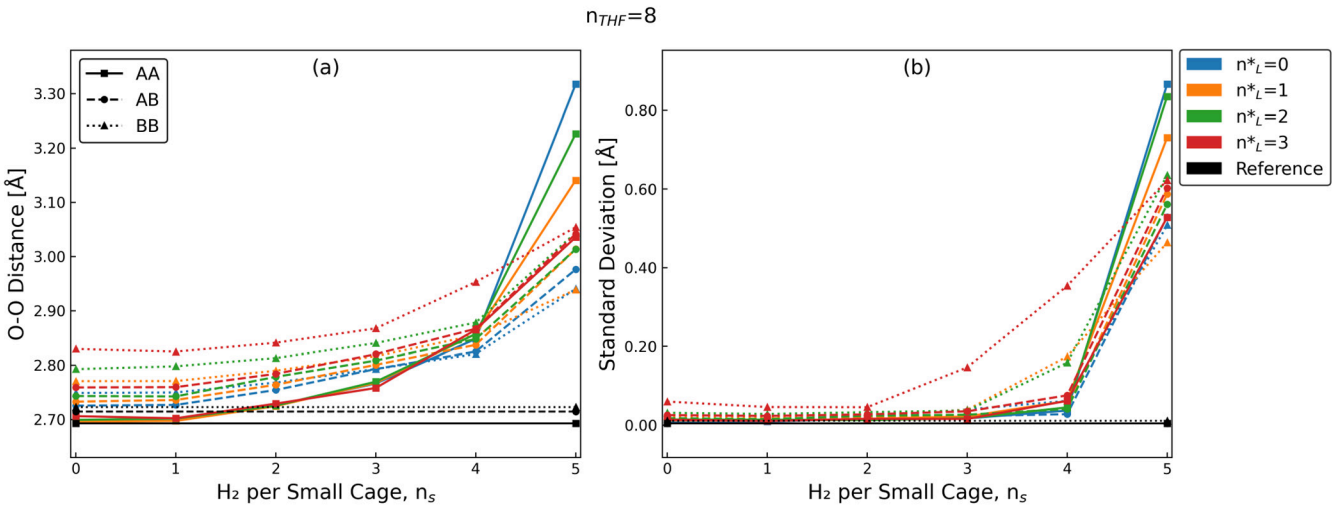


Figure 11. (**a**) Average O-O distances classified by the different types of oxygen atoms for stoichiometric compositions and (**b**) the standard deviations of the distributions. The reference lines indicate the average values of the different O-O distances and their corresponding standard deviations based on the empty sII hydrate structure, as tabulated in Table S3 of the Supplementary Materials.

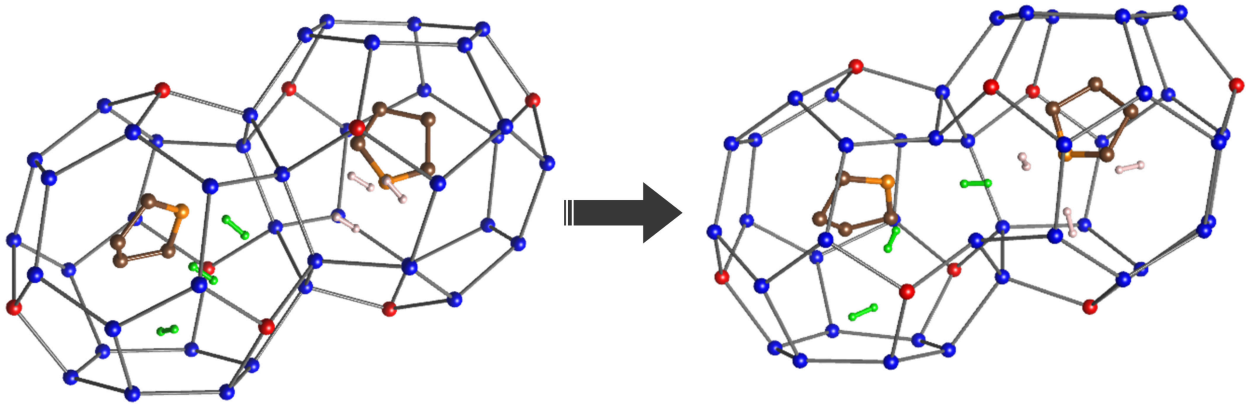


Figure 12. An instance of H_2 relocation between a pair of large cages in a structure of stoichiometric composition corresponding to $n_s = 3$, $n^*_L = 3$, and $n_{THF} = 8$. The cage pair prior to relaxation is shown to the left of the arrow, and the converged structure appears on the right. The green H_2 molecules are those initially belonging to the leftmost large cage of the pair. The white H_2 molecules originate from the rightmost large cage of the pair. The red and blue spheres represent class A and class B oxygen atoms, respectively. The orange spheres are the oxygens of THF. The THF and water hydrogens are hidden for clarity.

For the case of $n^*_L = 3$, the increased strain on the large cages due to high H_2 co-occupancy causes shifting of H_2 between large cages through the hexagonal faces, as illustrated in Figure 12, explaining the widened distribution of B-B distances even at lower small-cage occupancies.

3.2.3. O-H Covalent Bond and Hydrogen Bond Lengths

The O-H covalent bond length is defined as the interatomic distance between an oxygen and a hydrogen atom within the same water molecule. The hydrogen bond lengths are labelled O-H—O such that the leftmost oxygen in the notation is that which the hydrogen atom is covalently bonded to, and the rightmost oxygen atom is that which

the hydrogen is hydrogen-bonded to. The hydrogen bond length measured is the distance between the hydrogen atom and the oxygen it is hydrogen-bonded to. Due to the nature of these interactions, that is the covalent bonds being chemical in nature while the hydrogen bonds are physical, the covalent bonds are inherently stronger than hydrogen bonds. The inverse relation between bond strength and length means that the covalent bonds are, on average, shorter than hydrogen bonds, which is evident from Figures 13–15.

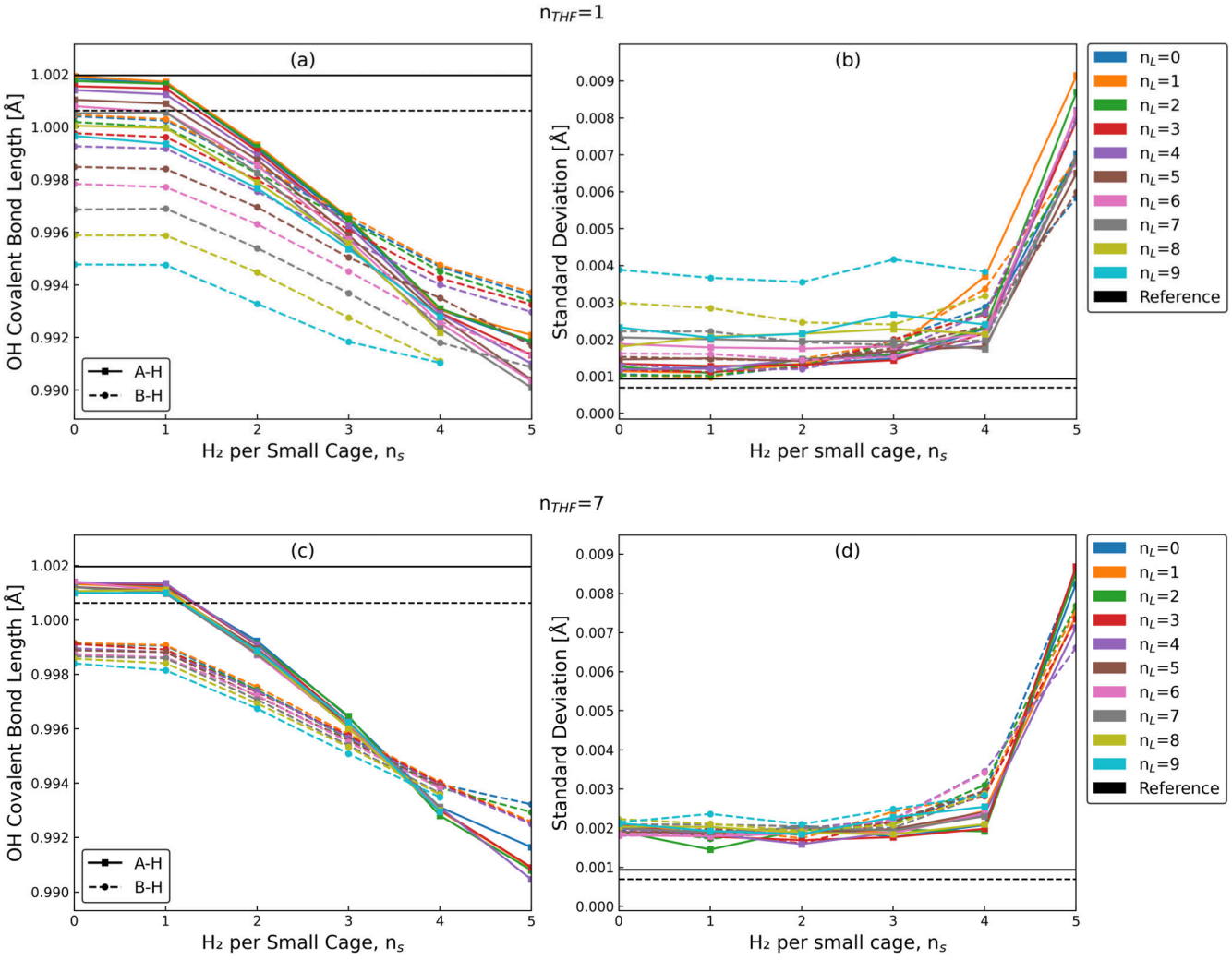


Figure 13. Average O-H covalent bond lengths classified by the different types of oxygen atoms for nonstoichiometric compositions corresponding to a THF loading of (**a**) 1 and (**c**) 7 and their standard deviations (**b**,**d**). The reference lines indicate the average values of the different covalent bond lengths and their corresponding standard deviations based on the empty sII hydrate structure, as tabulated in Table S3 of the Supplementary Materials.

Furthermore, the covalent and hydrogen bond strengths are linked through a compensation mechanism such that the stronger the hydrogen bonds, the weaker the covalent bonds are due to water's hydrogen atoms being pulled away from the oxygen center by these strong hydrogen bond interactions, thus elongating the covalent bonds. This explains the opposing trends observed between Figures 13 and 14, and between Figure 15a,c whereby the covalent bond lengths decrease (grow stronger) as the hydrogen bond lengths increase (grow weaker) due to the water molecules moving further apart under expansion. This compensation mechanism was also reported for other gas hydrate systems, including for sI methane hydrates, sII hydrocarbon hydrates, binary sH hydrates, and pure sII hydrogen hydrates [8,51,53,54].

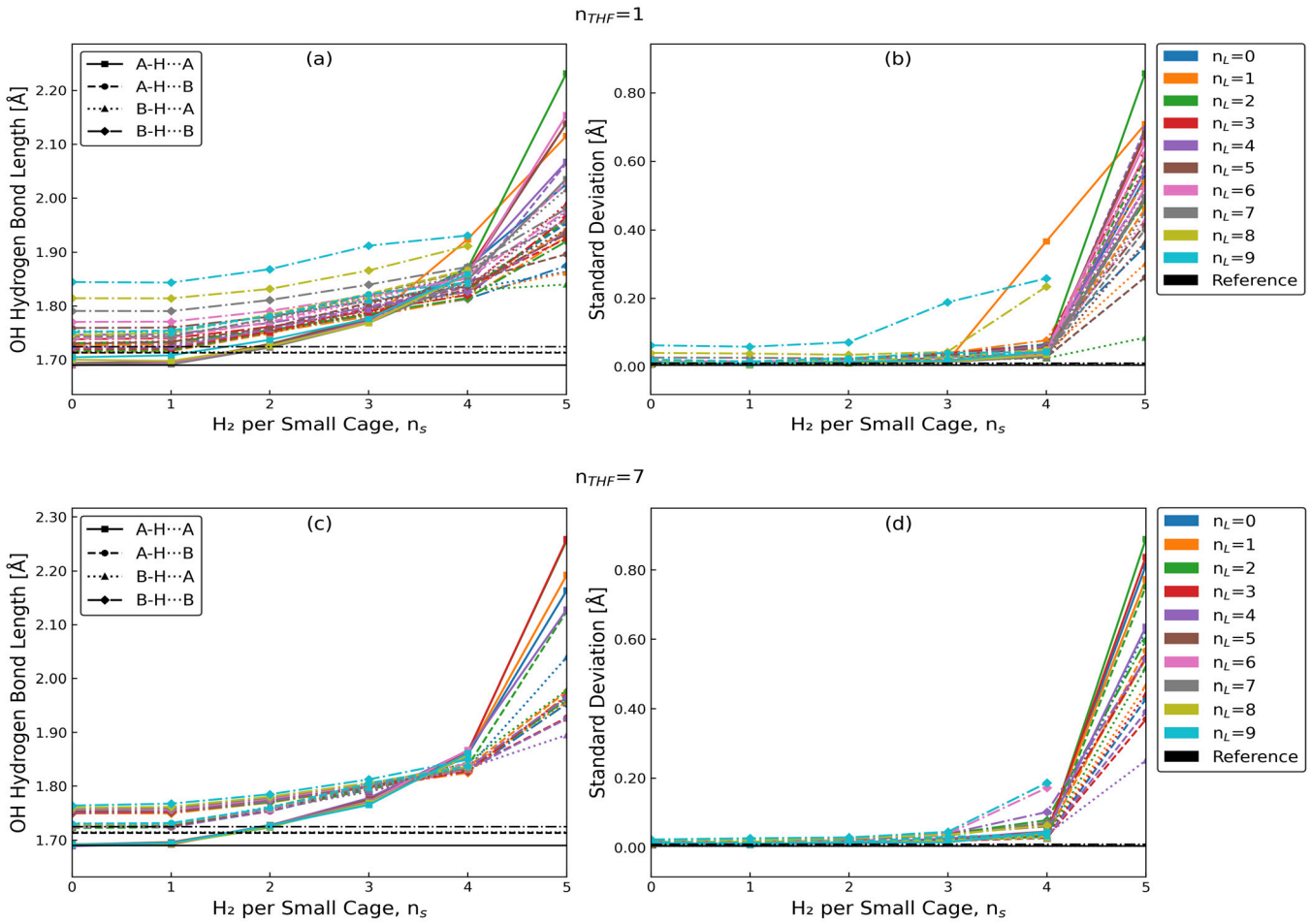


Figure 14. Average O-H hydrogen bond lengths classified by the different types of oxygen atoms for nonstoichiometric compositions corresponding to a THF loading of (**a**) 1 and (**c**) 7 and their standard deviations (**b**,**d**). The reference lines indicate the average values of the different hydrogen bond lengths and their corresponding standard deviations based on the empty sII hydrate structure, as tabulated in Table S3 of the Supplementary Materials.

The two different types of covalent bond lengths, A-H and B-H, have different baselines as determined from the empty sII hydrate, with the B-H bonds averaging to shorter lengths. This is a consequence of the imposed geometries in the sII hydrate framework associated with the cage shapes and sizes, with the water molecules pertaining to large cages being more spaced out on average to allow for larger hexagonal faces to exist, while the water molecules making up the small cages are able to exist more compactly as is also observed from the O-O distances trends. With the large-cage water molecules being mostly B-type oxygen based, this results in the B-H covalent bonds being slightly shorter due to the B-type containing water molecules being slightly less bound to each other.

The lengths of the covalent bonds are further impacted once guest molecules come into play causing all around expansion. Both covalent bond types grow shorter with increasing small-cage and large-cage occupancies, but the A-H bonds are more sensitive to small-cage occupancy, as illustrated by the steeper slopes in Figure 13a,c, while the B-H bonds are more sensitive to large-cage occupancy, as given by the wider vertical spacing between their level curves. This behaviour is also observed for the hydrogen bond lengths as shown in Figure 14. The hydrogen bond types that are more concentrated in the large cages' environments are the ones that average to larger values than those linking water molecules of small cages due to the compensation mechanism discussed earlier.

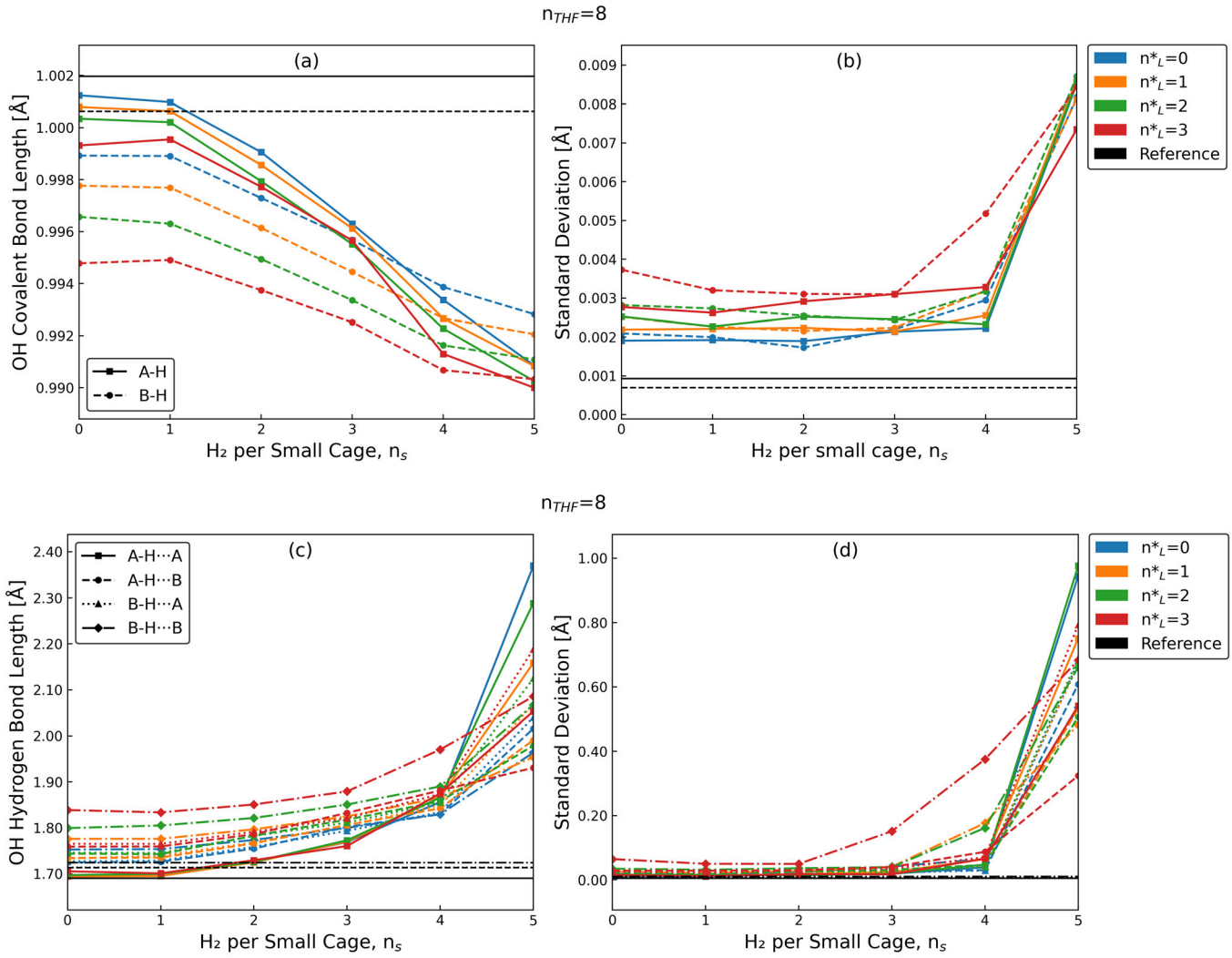


Figure 15. (**a**) Average O-H covalent bond lengths and (**c**) hydrogen bond lengths classified by the different types of oxygen atoms for stoichiometric compositions, and their standard deviations (**b**,**d**). The reference lines indicate the average values and their corresponding standard deviations based on the empty sII hydrate structure, as tabulated in Table S3 of the Supplementary Materials.

The widening of the O-H covalent and hydrogen bond distributions for nonstoichiometric compositions becomes most significant for small-cage occupancies above 4, in line with the O-O distance and cage volume distributions.

Similar trends are observed for stoichiometric compositions in addition to the B-H covalent bonds and B-H—B hydrogen bonds showing wide distributions for compositions corresponding to $n_L^* = 3$ due to the deformation of hexagonal faces in large cages.

3.2.4. O-O-O Angles

The O-O-O angle is the angle subtended at the central oxygen atom by two neighbouring oxygen atoms in the hydrate framework. Reference values are taken from the empty sII hydrate to capture the intrinsic geometry of the lattice backbone before any perturbation is induced by guest molecules. Although a regular pentagon and hexagon have internal angles of 108° and 120°, respectively, the polygonal faces in the sII lattice deviate from these ideal values. The lattice connectivity forces many water oxygen centers to be part of pentagonal and hexagonal faces simultaneously via shared edges, and the water molecules must also satisfy local tetrahedral coordination according to the Bernal-Fowler ice rules [55].

These competing geometric constraints therefore distort the face angles away from the regular-polygon values.

Hexagonal faces only contain BBB angles, which average the highest with a range reaching the typical internal angle of a regular hexagon at 120°. Pentagonal faces shared between small and large cages contain BBB, ABB, and BAB angles, the last of which is unique to these pentagonal faces; pentagonal faces shared only between small cages contain ABB, AAA, and AAB angles, the last two being unique to these types of pentagonal faces. Evidently, the angles that are characteristic of pentagonal faces shared between small cages have the three lowest averages in Figure 16, and their ranges fall around the 108° standard for a regular pentagon. The pentagonal face BAB angle is the most deviated from the 108° ideal due to the influence of the nearby hexagonal faces.

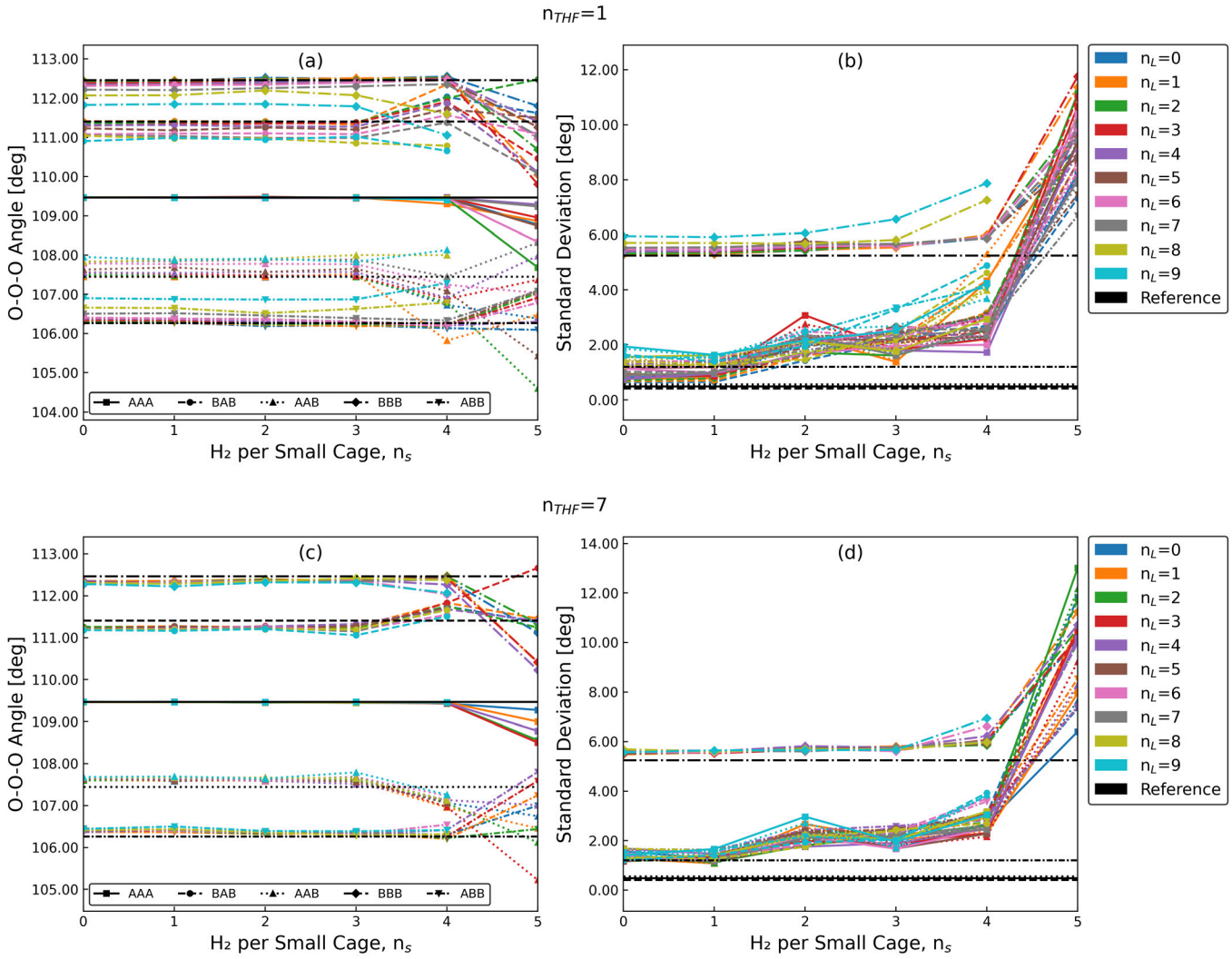


Figure 16. Average O-O-O angles classified by the different types of oxygen atoms for nonstoichiometric compositions corresponding to a THF loading of (**a**) 1 and (**c**) 7 and their standard deviations (**b**,**d**). The reference lines indicate the average values and their corresponding standard deviations based on the empty sII hydrate structure, as tabulated in Table S3 of the Supplementary Materials.

The O-O-O distributions for nonstoichiometric compositions show minimal variation with H_2 cage occupancies and remain close to their respective baselines up to the small-cage occupancy that is characteristic of increasing standard deviations. Over the same range of occupancies where the O-O-O angles show minimal offsetting from the baseline, other properties, such as the O-O distances and O-H covalent and hydrogen bond lengths vary

in accordance with cage expansion. This indicates that the water molecules maintain the orientation that is characteristic to their local environment's geometry during this expansion until the binding forces between them grow weak enough. Similar trends are observable for the stoichiometric compositions as shown in Figure 17, with evidence of large cage deformation at low small-cage occupancies when $n_L^* = 3$.

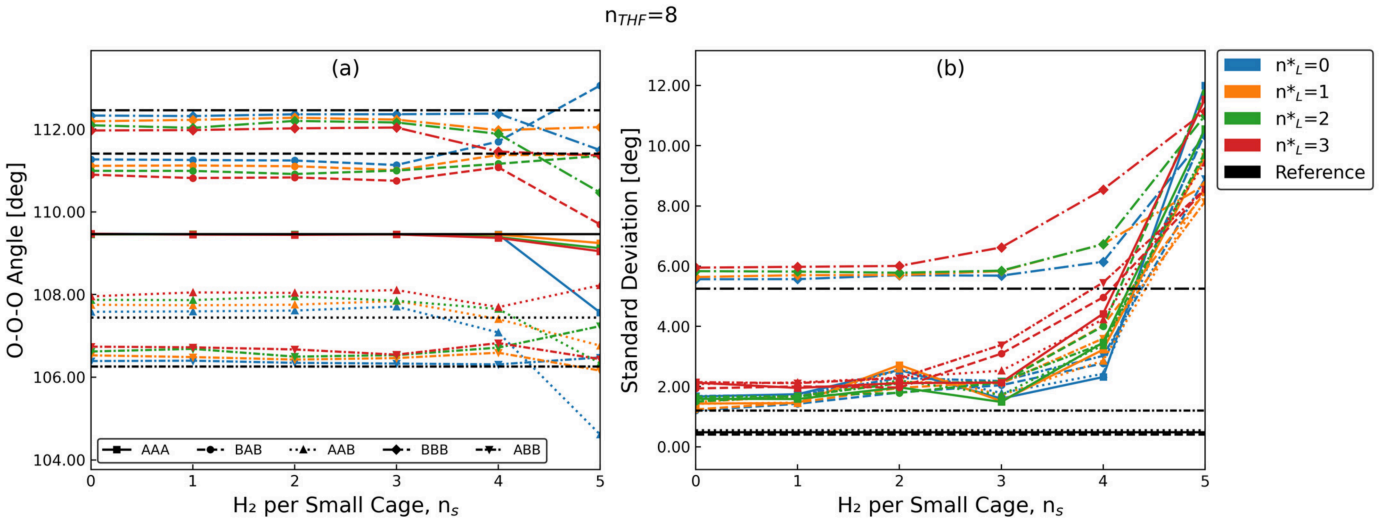


Figure 17. (**a**) Average O-O-O angles classified by the different types of oxygen atoms for stoichiometric compositions and (**b**) their standard deviations. The reference lines indicate the average values and their corresponding standard deviations based on the empty sII hydrate structure, as tabulated in Table S3 the Supplementary Materials.

4. Discussion

4.1. Failure Mechanisms

The energy analysis of Section 3.1 was the first to give us insight on how the binary system depends on small- and large-cage H_2 occupancies as well as the THF loading. It revealed the binding nature of the THF molecules, which grew stronger with THF loading, thus contributing to the overall stability of the converged structures in compensation for the growing repulsive forces induced by increasing H_2 occupancy. The energy analysis also reveals a common trend observed in all subsequent analyses of geometric properties of nonstoichiometric compositions and that is the sensitivity of a given property to large-cage H_2 occupancy decreases as the THF loading increases owing to there being a smaller fraction of hydrogen-occupied large cages that are too dispersed throughout the structure to bring about significant structural change beyond their local environments. On the other hand, small-cage H_2 occupancy affects properties in the same way regardless of THF loading or large-cage H_2 filling. Furthermore, the observed deviations away from the established energy trends or the lack of convergence of structures beyond specific H_2 occupancies are signs that those occupancies are thresholds to the mechanism in action to accommodate additional H_2 guests, the nature of which becomes clearer upon further inspection of geometric properties across the structure.

Inspection of small- and large-cage volumes across compositions reveals the primary mechanism that mitigates the growing repulsive forces with increasing H_2 occupancy: overall lattice expansion. Both cage types expand to create additional free volume for guest molecules and respond to increased repulsion. However, the emergence of markedly broader cage volume distributions at the same occupancy thresholds identified in the energy analysis shows that this expansion is not indefinitely uniform. The initially smooth expansion that occurs as occupancy increases from zero gives way beyond a threshold to

heterogeneous responses that produce wide distributions. This motivates investigations of interatomic distance and angle distributions to clarify the atomistic mechanisms operating past those thresholds.

Analysis of O-O separations further supports the expansion mechanism based on the positive trend between O-O distances and H_2 occupancy. Classifying O-O types by the participating oxygen atoms shows that, for both stoichiometric and nonstoichiometric compositions, deformation initiates in the small cages once small-cage occupancy exceeds four H_2 molecules. For stoichiometric systems, large cage deformation appears when the co-occupancy reaches $n_L^* = 3$; in nonstoichiometric systems, THF-free large cages tolerate much higher H_2 loadings (on the order of 8 or 9) before comparable distortions occur. These observations mark the emergence of a secondary deformation mode, one in which water molecules become sufficiently separated that hydrogen-bonding weakens, facilitating increased angular reorientation and positional shifting during relaxation, which opens polygonal faces and drives cages away from their standard conformations.

These postulates are further supported by the O-H covalent and hydrogen bond length distributions as well as the O-O-O angle distributions. We observe the growth of the hydrogen bond length, linked to their weakening, and the corresponding compensatory reduction in covalent bond lengths, linked to their strengthening, in line with expansion, and that the hydrogen bond lengths, especially the types associated mostly with small cages, grow far away from the standard baseline as small-cage occupancy increases, indicating the onset of local structural disorder that is not characteristic of a crystalline lattice structure. Finally, the fact that the O-O-O angles are relatively invariant up to the point where all the previous properties have been seen to have widened distributions is the ultimate confirmation that this is caused by the reorientation of water molecules away from their ordered state.

In retrospect, while cage expansion eventually brings about local deformation, it creates more free space which hydrogens from overcrowded cages can relocate to minimize repulsive forces. This relocation of hydrogens to regions of lower concentration mitigates the proliferation of deformations before leading to complete structural failure. For both stoichiometric and nonstoichiometric compositions, deformation initiates in the small cages when n_s exceeds 4, suggesting that this is the occupancy limit for small cages; at that point, some hydrogens relocate from small cages into adjacent large cages through their shared pentagonal faces. In nonstoichiometric compositions, the THF-free large cages can sustain very high H_2 occupancies and only begin to deform when n_L approaches 8 or 9. By contrast, in stoichiometric compositions, THF-occupied large cages cannot accommodate as many H_2 molecules, and deformation is most prominent at those cages once co-occupancy reaches $n_L^* = 3$. When deformations are localized to the large cages, H_2 relocation through hexagonal faces is promoted during geometric optimization.

Because higher THF loadings increase the promoter's binding contribution and reduce the structure's sensitivity to large-cage H_2 occupancy, the absolute values of structural and energetic properties differ between THF loadings even when n_s and n_L (or n_L^*) are held constant. What does not change, however, are the overall trends observed and the system's two-step response to occupancy-driven strain. Across the compositions we studied, the systems follow the same response mechanism outlined previously, and the small- and large-cage occupancy thresholds remain at comparable levels. Thus, within the zero Kelvin DFT framework used here, future computational studies of the H_2-THF binary hydrate could reduce the test pool to compositions at a single representative THF loading since the trends and the system's response to applied stimuli are equivalently captured across different THF loadings. Choosing which THF loading will be most worthwhile to pursue is an optimization problem, one that strikes a balance between the thermodynamic promotion

gained from additional THF against the loss in hydrogen capacity that accompanies higher promoter capacity, as explored in the following section.

4.2. Storage Capacity

Based on the distributions and standard deviations presented in Section 3, we establish maximum theoretical thresholds for the H_2 storage capacity in H_2-THF binary hydrates. The approach used to select the compositions representative of these thresholds is to choose the compositions with maximum storage capacity that fall just outside the regions where standard deviations and distributions start to widen to avoid where the structures start to significantly deform either at the small or large cages. For stoichiometric hydrates, this representative composition is $3H_2(S)$-$2H_2(L)$-8THF. For nonstoichiometric hydrates, the maximum theoretical storage capacity depends on the THF loading. The representative compositions for each THF loading scheme are as follows:

- $4H_2(S)$-$7H_2(L)$-1THF;
- $4H_2(S)$-$8H_2(L)$-2THF;
- $4H_2(S)$-$8H_2(L)$-3THF;
- $4H_2(S)$-$7H_2(L)$-4THF;
- $4H_2(S)$-$7H_2(L)$-5THF;
- $4H_2(S)$-$7H_2(L)$-6THF;
- $4H_2(S)$-$8H_2(L)$-7THF.

As presented in Figure 18, even at the lowest THF loading of $n_{THF} = 1$, the maximum theoretical storage capacity of the binary hydrate (8.28 wt%) falls short of that for pure H_2 hydrates (9.53 wt%) [8] As the THF loading increases to $n_{THF} = 7$, the maximum possible storage capacity for nonstoichiometric binary hydrates decreases toward 4.68 wt%, which still exceeds that of stoichiometric binary hydrates ($n_{THF} = 8$) at 4.09 wt%. Therefore, for the binary H_2-THF hydrates to exceed the ultimate DOE target placed at 6.50 wt%, the composition must be nonstoichiometric with $n_{THF} \leq 3$. While we have shown that these hydrates are thermodynamically favourable to form, it is difficult to exercise this level of control over cage occupancy, and thus composition, in practice since that relies on several factors such as the preparation method and formation conditions used, the impacts of which are beyond the scope of this study. Nevertheless, our 0 K DFT results define the theoretical upper limit of storage capacity in these binary hydrates and capture the fundamental base response of the structures to occupancy, as evidenced by the agreement between the trends in this study and those reported in positive-temperature MD studies [26,31]. This validity at non-zero temperatures stems from the fact that the potential energy surface, which is the primary driver of lattice geometry, remains relatively unchanged at finite temperatures [56]. The bottom-up computational approach employed here serves as a predictive framework that can guide future experimental efforts to design and reverse-engineer optimized clathrate storage media.

Under practical operating conditions at finite temperatures, the inclusion of thermal and kinetic energy introduces lattice fluctuations that can result in the structural deformations observed in this study occurring at lower occupancy limits. To quantitatively capture these thermal effects, the ground-state configurations established in this work can serve as a direct baseline for subsequent lattice dynamics evaluations. Specifically, these zero-Kelvin results can be extended to finite temperatures through phonon calculations using approaches like the finite displacement method, or density functional perturbation theory (DFPT) [57–61].

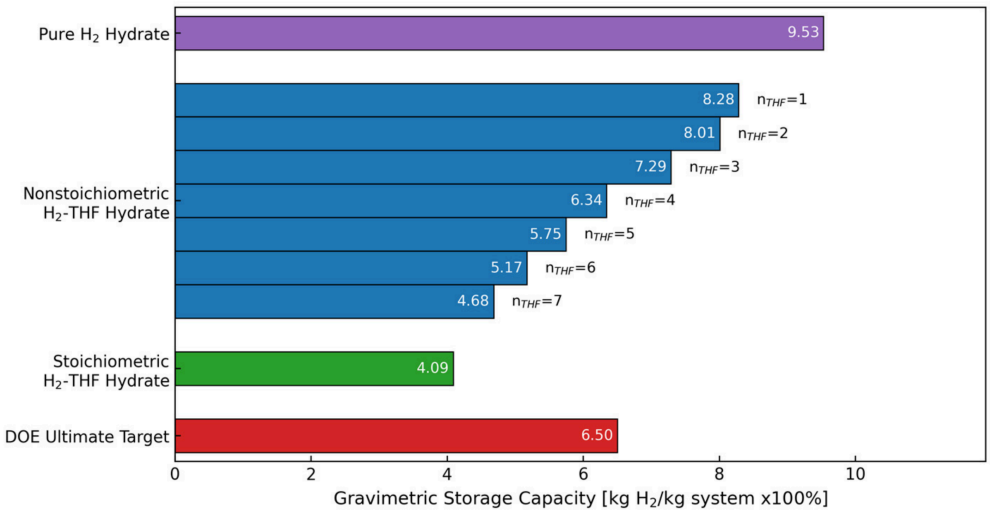


Figure 18. Storage capacity thresholds (in wt%) for stoichiometric and nonstoichiometric binary H_2-THF hydrates from this work and pure H_2 hydrates reported by Sofla et al. in comparison to the ultimate DOE target for onboard hydrogen storage for light-duty fuel cell vehicles [8,9].

Additionally, because these static simulations are performed at 0 K, the guest-host configurations explored here can be stable at zero external pressure due to the absence of thermal vibrations. On the other hand, under practical operating conditions, finite temperatures would necessitate external pressures to stabilize these structures, the exact quantification of which requires thermodynamic equilibrium mapping beyond the scope of static zero-Kelvin DFT calculations. Moreover, future investigations incorporating pressure effects would be highly valuable to explore how external compressive pressure balances guest-induced framework expansion, potentially shifting the structural thresholds to accommodate higher guest occupancies.

While lower promoter loadings like $n_{THF} = 1$ maximize hydrogen capacity in these binary hydrate systems, they inherently diminish the thermodynamic promotion effect, shifting the required formation and stabilization pressures closer to the extreme conditions of pure H_2 hydrates. Referring back to the recommendation to limit the composition set for future investigations, the ideal THF loading to consider is $n_{THF} = 3$. This is the highest promoter loading at which the DOE's ultimate target can theoretically be exceeded and therefore represents the maximum promoter benefit compatible with practical H_2 capacity goals.

5. Conclusions

This zero Kelvin DFT study explores how guest occupancy affects H_2-THF hydrate structures and highlights a two-step response mechanism: an initial uniform lattice expansion that accommodates additional guests while preserving structural integrity, followed by pronounced deformation that signals incipient structural breakdown. In nonstoichiometric compositions, destabilization typically begins at small cages once $n_s > 4$, with THF-free large cages only deforming at very high H_2 loadings ($n_L \approx 8 - 9$). In stoichiometric compositions, large-cage deformation occurs at much lower H_2 occupancies because those cages are also shared with THF, while small-cage threshold remains similar. Based on these established ceilings for occupancy limits, we conclude that the stoichiometric hydrates, even at their theoretical maximum, do not meet the DOE hydrogen storage criteria for light-duty vehicles, whereas nonstoichiometric compositions can exceed this standard provided that THF loading is sufficiently low ($n_{THF} \leq 3$).

Supplementary Materials: The following supporting information can be downloaded at: https://www.mdpi.com/article/10.3390/en19133023/s1, Figure S1: The converged total energy and elapsed time using $1 \times 1 \times 1$ and $2 \times 2 \times 2$ k-point grids; Figure S2: The converged total energy and elapsed time using an EDIFF of 1×10^{-4}, 1×10^{-6}, 1×10^{-8}, and 1×10^{-12} eV; Figure S3: The converged total energy and elapsed time using an ENCUT of 520, 600, 650, and 700 eV; Figure S4: The converged total energy and elapsed time using a $1 \times 1 \times 1$ unit cell and a $2 \times 2 \times 2$ supercell; Figure S5: The converged total energy and elapsed time using RMM-DIIS (IBRION = 1) and CGA (IBRION = 2) geometric relaxation algorithms; Figure S6: The converged total energy and the total memory utilized using RMM-DIIS (IBRION = 1) and CGA (IBRION = 2) geometric relaxation algorithms; Figure S7: The energy-volume data for THF hydrate obtained from our study fitted with the Vinet EOS; Figure S8: The energy-volume data for H_2 hydrate (4S1L) obtained from our study fitted with the Murnaghan EOS; Figure S9: Cohesive energies for different THF loading schemes; Figure S10: The binding energies corresponding to incrementing the small-cage H_2 occupancy under different THF loadings; Figure S11: The binding energies corresponding to incrementing the large-cage H_2 occupancy for nonstoichiometric compositions under different THF loadings; Figure S12: The binding energies corresponding to incrementing the large-cage H_2 occupancy for stoichiometric compositions; Figure S13: Average small- and large-cage volumes for different THF loadings; Figure S14: Average O-O distances classified by the different types of oxygen atoms for different THF loadings and their standard deviations; Figure S15: Average O-H covalent bond lengths classified by the different types of oxygen atoms for different THF loadings and their standard deviations; Figure S16: Average O-H hydrogen bond lengths classified by the different types of oxygen atoms for different THF loadings and their standard deviations; Figure S17: Average O-O-O angles classified by the different types of oxygen atoms for different THF loadings and their standard deviations; Figure S18: Average H-O-H angles classified by the different types of oxygen atoms for different THF loadings and their standard deviations; Figure S19: Average hydrogen bond angles classified by the different types of oxygen atoms for different THF loadings and their standard deviations; Table S1: The Vinet EOS fitting parameters for the pure sII THF hydrate system; Table S2: The Murnaghan EOS fitting parameters for the pure sII H_2 hydrate system (4S1L case); Table S3: The mean values (m) and standard deviations (σ) of different structural parameters characteristic of the empty sII hydrate; Table S4: The total energies for symmetrically inequivalent placements of THF within large cages in the sII unit cell for the nonstoichiometric H_2-THF hydrate compositions corresponding to a THF loading of 1. Refs. [62,63].

Author Contributions: Conceptualization, M.W.M., S.M., A.D.R. and P.S.; methodology, M.W.M. and S.M.; software, M.W.M. and S.M.; validation, M.W.M.; formal analysis, M.W.M. and S.M.; investigation, M.W.M.; resources, A.D.R. and P.S.; data curation, M.W.M. and S.M.; writing—original draft preparation, M.W.M.; writing—review and editing, M.W.M., S.M., A.D.R. and P.S.; visualization, M.W.M.; supervision, A.D.R. and P.S.; project administration, A.D.R. and P.S.; funding acquisition, A.D.R. and P.S. All authors have read and agreed to the published version of the manuscript.

Funding: This research was funded by the Natural Sciences and Engineering Research Council of Canada Discovery under grant numbers 2983 and 42069-0, and the Graduate Excellence Award number 00152.

Data Availability Statement: The original contributions presented in this study are included in the article/Supplementary Material. Further inquiries can be directed to the corresponding authors.

Acknowledgments: This work was supported by the Fonds de Recherche du Québec Nature et Technologies through the Bourse de Maîtrise en Recherche. This research was enabled, in part, by the support provided by Calcul Québec, the BC DRI Group, and the Digital Research Alliance of Canada.

Conflicts of Interest: The authors declare no conflicts of interest.

Abbreviations

The following abbreviations are used in this manuscript:

DOE (U.S.) Department of Energy

THF	Tetrahydrofuran
DFT	Density functional theory
DFPT	Density functional perturbation theory
vdW	van der Waals
sI	Structure I
sII	Structure II
sH	Structure H
NMR	Nuclear magnetic resonance
MD	Molecular dynamics
GCMC	Grand canonical Monte Carlo
VASP	Vienna ab initio simulation package
CGA	Conjugate gradient algorithm
PAW	Projector-augmented-wave
revPBE	Revised Perdew-Burke-Ernzerhof
XC	Exchange-correlation

References

1. Carroll, J. *Natural Gas Hydrates: A Guide for Engineers [Internet]*, 3rd ed.; Gulf Professional Publishing: Boston, MA, USA, 2014. [CrossRef]
2. Li, Q.; Liu, J.; Wang, S.; Guo, Y.; Han, X.; Li, Q.; Cheng, Y.; Dong, Z.; Li, X.; Zhang, X. Numerical insights into factors affecting collapse behavior of horizontal wellbore in clayey silt hydrate-bearing sediments and the accompanying control strategy. *Ocean Eng.* **2024**, *297*, 117029. [CrossRef]
3. Qingchao, L.; Jingjuan, W.; Qiang, L.; Fuling, W.; Yuanfang, C. Sediment Instability Caused by Gas Production from Hydrate-Bearing Sediment in Northern South China Sea by Horizontal Wellbore: Sensitivity Analysis. *Nat. Resour. Res.* **2025**, *34*, 1667–1699. [CrossRef]
4. Li, Q.; Li, Q.; Wu, J.; He, K.; Xia, Y.; Liu, J.; Wang, F.; Cheng, Y. Wellhead Stability During Development Process of Hydrate Reservoir in the Northern South China Sea: Sensitivity Analysis. *Processes* **2025**, *13*, 1630. [CrossRef]
5. Sugahara, T.; Haag, J.C.; Prasad, P.S.R.; Warntjes, A.A.; Sloan, E.D.; Sum, A.K.; Koh, C.A. Increasing Hydrogen Storage Capacity Using Tetrahydrofuran. *J. Am. Chem. Soc.* **2009**, *131*, 14616–14617. [CrossRef] [PubMed]
6. Mao, W.L.; Mao, H.K.; Goncharov, A.F.; Struzhkin, V.V.; Guo, Q.; Hu, J.; Shu, J.; Hemley, R.J.; Somayazulu, M.; Zhao, Y. Hydrogen Clusters in Clathrate Hydrate. *Science* **2002**, *297*, 2247–2249. [CrossRef] [PubMed]
7. Di Profio, P.; Arca, S.; Rossi, F.; Filipponi, M. Comparison of hydrogen hydrates with existing hydrogen storage technologies: Energetic and economic evaluations. *Int. J. Hydrogen Energy* **2009**, *34*, 9173–9180. [CrossRef]
8. Jafari Daghalian Sofla, S.; Rey, A.D.; Servio, P. Atomistic Investigation of the occupancy limits and stability of hydrogen hydrates as a hydrogen storage medium. *Int. J. Hydrogen Energy* **2024**, *51*, 184–192. [CrossRef]
9. U.S. Department of Energy. Energy.Gov [Internet]. DOE Technical Targets for Onboard Hydrogen Storage for Light-Duty Vehicles. Available online: https://www.energy.gov/eere/fuelcells/doe-technical-targets-onboard-hydrogen-storage-light-duty-vehicles (accessed on 20 September 2025).
10. Alavi, S.; Ripmeester, J.A.; Klug, D.D. Molecular-dynamics simulations of binary structure II hydrogen and tetrahydrofurane clathrates. *J. Chem. Phys.* **2006**, *124*, 014704. [CrossRef] [PubMed]
11. Hester, K.C.; Strobel, T.A.; Sloan, E.D.; Koh, C.A.; Huq, A.; Schultz, A.J. Molecular Hydrogen Occupancy in Binary THF−H2 Clathrate Hydrates by High Resolution Neutron Diffraction. *J. Phys. Chem. B* **2006**, *110*, 14024–14027. [CrossRef] [PubMed]
12. Papadimitriou, N.I.; Tsimpanogiannis, I.N.; Papaioannou, A.T.; Stubos, A.K. Evaluation of the Hydrogen-Storage Capacity of Pure H2 and Binary H_2-THF Hydrates with Monte Carlo Simulations. *J. Phys. Chem. C* **2008**, *112*, 10294–10302. [CrossRef]
13. Majid, A.A.A.; Worley, J.; Koh, C.A. Thermodynamic and Kinetic Promoters for Gas Hydrate Technological Applications. *Energy Fuels* **2021**, *35*, 19288–19301. [CrossRef]
14. Florusse, L.J.; Peters, C.J.; Schoonman, J.; Hester, K.C.; Koh, C.A.; Dec, S.F.; Marsh, K.N.; Sloan, E.D. Stable Low-Pressure Hydrogen Clusters Stored in a Binary Clathrate Hydrate. *Science* **2004**, *306*, 469–471. [CrossRef] [PubMed]
15. Manakov, A.Y.; Goryainov, S.V.; Kurnosov, A.V.; Likhacheva, A.Y.; Dyadin, Y.A.; Larionov, E.G. Clathrate Nature of the High-Pressure Tetrahydrofuran Hydrate Phase and Some New Data on the Phase Diagram of the Tetrahydrofuran−Water System at Pressures up to 3 GPa. *J. Phys. Chem. B* **2003**, *107*, 7861–7866. [CrossRef]
16. Hashimoto, S.; Murayama, S.; Sugahara, T.; Sato, H.; Ohgaki, K. Thermodynamic and Raman spectroscopic studies on H_2 + tetrahydrofuran + water and H_2 + tetra-n-butyl ammonium bromide + water mixtures containing gas hydrates. *Chem. Eng. Sci.* **2006**, *61*, 7884–7888. [CrossRef]

17. Strobel, T.A.; Koh, C.A.; Sloan, E.D. Thermodynamic predictions of various tetrahydrofuran and hydrogen clathrate hydrates. *Fluid Phase Equilibria* **2009**, *280*, 61–67. [CrossRef]
18. Seo, Y.T.; Kang, S.P.; Lee, H. Experimental determination and thermodynamic modeling of methane and nitrogen hydrates in the presence of THF, propylene oxide, 1,4-dioxane and acetone. *Fluid Phase Equilibria* **2001**, *189*, 99–110. [CrossRef]
19. Kang, S.P.; Lee, H.; Lee, C.S.; Sung, W.M. Hydrate phase equilibria of the guest mixtures containing CO_2, N_2 and tetrahydrofuran. *Fluid Phase Equilibria* **2001**, *185*, 101–109. [CrossRef]
20. Mi, F.; Ning, F.; Vlugt, T.J.H.; Moultos, O.A. Molecular insight into hydrogen storage in clathrate hydrates: The effect of different promoters on the spontaneous nucleation of hydrogen hydrates studied via microsecond-scale molecular dynamics simulations. *Chem. Eng. J.* **2025**, *512*, 162253. [CrossRef]
21. Strobel, T.A.; Taylor, C.J.; Hester, K.C.; Dec, S.F.; Koh, C.A.; Miller, K.T.; Sloan, E.D. Molecular Hydrogen Storage in Binary THF−H2 Clathrate Hydrates. *J. Phys. Chem. B* **2006**, *110*, 17121–17125. [CrossRef] [PubMed]
22. Udachin, K.A.; Lipkowski, J.; Tkacz, M. Double clathrate hydrates with helium and hydrogen. *Supramol. Chem.* **1994**, *3*, 181–183. [CrossRef]
23. Talyzin, A. Feasibility of H_2-THF-H_2O clathrate hydrates for hydrogen storage applications. *Int. J. Hydrogen Energy* **2008**, *33*, 111–115. [CrossRef]
24. Chun, D.H.; Lee, T.Y. Molecular simulation of cage occupancy and selectivity of binary THF–H2 sII hydrate. *Mol. Simul.* **2008**, *34*, 837–844. [CrossRef]
25. Kaur, S.P.; Ramachandran, C.N. Hydrogen-tetrahydrofuran mixed hydrates: A computational study. *Int. J. Hydrogen Energy* **2018**, *43*, 19559–19566. [CrossRef]
26. Liu, J.; Hou, J.; Xu, J.; Liu, H.; Chen, G.; Zhang, J. Ab initio study of the molecular hydrogen occupancy in pure H_2 and binary H2-THF clathrate hydrates. *Int. J. Hydrogen Energy* **2017**, *42*, 17136–17143. [CrossRef]
27. Lee, H.; Lee, J.W.; Kim, D.Y.; Park, J.; Seo, Y.T.; Zeng, H.; Moudrakovski, I.L.; Ratcliffe, C.I.; Ripmeester, J.A. Tuning clathrate hydrates for hydrogen storage. *Nature* **2005**, *434*, 743–746. [CrossRef] [PubMed]
28. Kim, D.Y.; Park, Y.; Lee, H. Tuning clathrate hydrates: Application to hydrogen storage. *Catal. Today* **2007**, *120*, 257–261. [CrossRef]
29. Hashimoto, S.; Sugahara, T.; Sato, H.; Ohgaki, K. Thermodynamic Stability of H_2 + Tetrahydrofuran Mixed Gas Hydrate in Nonstoichiometric Aqueous Solutions. *J. Chem. Eng. Data* **2007**, *52*, 517–520. [CrossRef]
30. Lokshin, K.A.; Zhao, Y.; He, D.; Mao, W.L.; Mao, H.K.; Hemley, R.J.; Lobanov, M.V.; Greenblatt, M. Structure and Dynamics of Hydrogen Molecules in the Novel Clathrate Hydrate by High Pressure Neutron Diffraction. *Phys. Rev. Lett.* **2004**, *93*, 125503. [CrossRef] [PubMed]
31. Zheng, R.; Mohammed, S.; Jia, Y.; Hazra, R.; Gadikota, G. The effect of H2 occupancy modes in small and large cages of H2 –tetrahydrofuran hydrates on the hydrates' stability and H_2 storage capacity. *Phys. Chem. Chem. Phys.* **2025**, *27*, 6532–6545. [CrossRef] [PubMed]
32. Kanaujiya, R.; Metya, A.K.; Choudhary, N.; Kumar, R.; Patra, T.K. Molecular dynamics insights into tetrahydrofuran-assisted formation of CH_4, CO_2, and H_2 gas hydrates. *Phys. Chem. Chem. Phys.* **2025**, *27*, 13991–13999. [CrossRef] [PubMed]
33. Zhang, J.; Cai, X.; Li, Y.; Gao, J.; Xiao, M.; Li, Y.; Wang, X.; Yin, Z. Unveiling how THF tunes the micro-kinetics of H_2-THF clathrate for enhanced H_2 storage: A molecular dynamics study. *J. Colloid Interface Sci.* **2026**, *705*, 139483. [CrossRef] [PubMed]
34. Kresse, G.; Furthmüller, J. Efficiency of ab-initio total energy calculations for metals and semiconductors using a plane-wave basis set. *Comput. Mater. Sci.* **1996**, *6*, 15–50. [CrossRef]
35. Kresse, G.; Furthmüller, J. Efficient iterative schemes for ab initio total-energy calculations using a plane-wave basis set. *Phys. Rev. B* **1996**, *54*, 11169–11186. [CrossRef] [PubMed]
36. Kresse, G.; Hafner, J. Ab initio molecular dynamics for liquid metals. *Phys. Rev. B* **1993**, *47*, 558–561. [CrossRef] [PubMed]
37. Kresse, G.; Joubert, D. From ultrasoft pseudopotentials to the projector augmented-wave method. *Phys. Rev. B* **1999**, *59*, 1758–1775. [CrossRef]
38. Sholl, D.S.; Steckel, J.A. *Density Functional Theory: A Practical Introduction [Internet]*; John Wiley & Sons, Inc.: Hoboken, NJ, USA, 2009; 243 p. Available online: https://onlinelibrary.wiley.com/doi/book/10.1002/9780470447710 (accessed on 2 August 2024).
39. Takeuchi, F.; Hiratsuka, M.; Ohmura, R.; Alavi, S.; Sum, A.K.; Yasuoka, K. Water proton configurations in structures I, II, and H clathrate hydrate unit cells. *J. Chem. Phys.* **2013**, *138*, 124504. [CrossRef] [PubMed]
40. Martínez, L.; Andrade, R.; Birgin, E.G.; Martínez, J.M. *Packmol: A Package for Building Initial Configurations for Molecular Dynamics [Internet]*; University of São Paulo: São Paulo, Brazil, 2009. Available online: https://m3g.github.io/packmol/citation.shtml (accessed on 2 August 2024).
41. Mathews, S.; Zhu, X.; Guerra, A.; Servio, P.; Rey, A. Atomistic Modeling of Methane and Carbon Dioxide Structure I Gas Hydrates under Pressure: Guest Effects and Properties. *J. Chem. Theory Comput.* **2026**, *22*, 3114–3124. [CrossRef] [PubMed]
42. Vlasic, T.M.; Servio, P.; Rey, A.D. Atomistic modeling of structure II gas hydrate mechanics: Compressibility and equations of state. *AIP Adv.* **2016**, *6*, 085317. [CrossRef]

43. Vlasic, T.M.; Servio, P.D.; Rey, A.D. THF Hydrates as Model Systems for Natural Gas Hydrates: Comparing Their Mechanical and Vibrational Properties. *Ind. Eng. Chem. Res.* **2019**, *58*, 16588–16596. [CrossRef]
44. Zhu, X.; Rey, A.D.; Servio, P. Piezo-elasticity and stability limits of monocrystal methane gas hydrates: Atomistic-continuum characterization. *Can. J. Chem. Eng.* **2023**, *101*, 639–650. [CrossRef]
45. Juan, J.; Longone, P.J.; Marchetti, J.M.; Pronsato, M.E.; Ramirez-Pastor, A.J. Theoretical study of CH4 intercalation in sI clathrate hydrates for energy storage. *Fluid Phase Equilibria* **2026**, *609*, 114751. [CrossRef]
46. Daghash, S.M.; Servio, P.; Rey, A.D. Structural properties of sH hydrate: A DFT study of anisotropy and equation of state. *Mol. Simul.* **2019**, *45*, 1524–1537. [CrossRef]
47. Blöchl, P.E. Projector augmented-wave method. *Phys. Rev. B* **1994**, *50*, 17953–17979. [CrossRef] [PubMed]
48. Volume Relaxation-VASP Wiki [Internet]. Available online: https://vasp.at/wiki/Volume_relaxation (accessed on 28 April 2026).
49. Grimme, S. Semiempirical GGA-type density functional constructed with a long-range dispersion correction. *J. Comput. Chem.* **2006**, *27*, 1787–1799. [CrossRef] [PubMed]
50. Zhang, Y.; Yang, W. Comment on "Generalized Gradient Approximation Made Simple". *Phys. Rev. Lett.* **1998**, *80*, 890. [CrossRef]
51. Mathews, S.; Zhu, X.; Guerra, A.; Servio, P.; Rey, A. Geometric Characterizations of Non-Uniform Structure I Methane Hydrate Behaviors Under Pressure. *Crystals* **2025**, *15*, 518. [CrossRef]
52. Gorman, P.D.; English, N.J.; MacElroy, J.M.D. Dynamical cage behaviour and hydrogen migration in hydrogen and hydrogen-tetrahydrofuran clathrate hydrates. *J. Chem. Phys.* **2012**, *136*, 044506. [CrossRef] [PubMed]
53. Vlasic, T.M.; Servio, P.D.; Rey, A.D. Effect of Guest Size on the Mechanical Properties and Molecular Structure of Gas Hydrates from First-Principles. *Cryst. Growth Des.* **2017**, *17*, 6407–6416. [CrossRef]
54. Daghash, S.M.; Servio, P.; Rey, A.D. Elastic properties and anisotropic behavior of structure-H (sH) gas hydrate from first principles. *Chem. Eng. Sci.* **2020**, *227*, 115948. [CrossRef]
55. Bernal, J.D.; Fowler, R.H. A Theory of Water and Ionic Solution, with Particular Reference to Hydrogen and Hydroxyl Ions. *J. Chem. Phys.* **1933**, *1*, 515–548. [CrossRef]
56. Giustino, F. *Materials Modelling Using Density Functional Theory: Properties and Predictions*, 1st ed.; Oxford University Press: Oxford, UK, 2014; 304 p.
57. Kresse, G.; Furthmüller, J.; Hafner, J. Ab initio Force Constant Approach to Phonon Dispersion Relations of Diamond and Graphite. *Eur. Lett.* **1995**, *32*, 729. [CrossRef]
58. Parlinski, K.; Li, Z.Q.; Kawazoe, Y. First-principles determination of the soft mode in cubic ZrO_2. *Phys. Rev. Lett.* **1997**, *78*, 4063–4066. [CrossRef]
59. Giannozzi, P.; de Gironcoli, S.; Pavone, P.; Baroni, S. Ab initio calculation of phonon dispersions in semiconductors. *Phys. Rev. B* **1991**, *43*, 7231–7242. [CrossRef] [PubMed]
60. Gonze, X.; Lee, C. Dynamical matrices, Born effective charges, dielectric permittivity tensors, and interatomic force constants from density-functional perturbation theory. *Phys. Rev. B-Condens. Matter Mater. Phys.* **1997**, *55*, 10355–10368. [CrossRef]
61. Mathews, S.L.; Servio, P.D.; Rey, A.D. Heat Capacity, Thermal Expansion Coefficient, and Grüneisen Parameter of CH4, CO2, and C_2H_6 Hydrates and Ice Ih via Density Functional Theory and Phonon Calculations. *Cryst. Growth Des.* **2020**, *20*, 5947–5955. [CrossRef]
62. Pandit, A.; Bongiorno, A. First-principles calculation of the pressure derivative of the bulk modulus from second- and third-order elastic constants. *Phys. Rev. Mater.* **2023**, *7*, 073801. [CrossRef]
63. Jafari Daghalian Sofla, S.; Servio, P.; Rey, A.D. Atomistic-geometry inspired structure-composition-property relations of hydrogen sII hydrates. *Sci. Rep.* **2023**, *13*, 19675. [CrossRef] [PubMed]

Disclaimer/Publisher's Note: The statements, opinions and data contained in all publications are solely those of the individual author(s) and contributor(s) and not of MDPI and/or the editor(s). MDPI and/or the editor(s) disclaim responsibility for any injury to people or property resulting from any ideas, methods, instructions or products referred to in the content.